First results from 2 + 1 dynamical quark flavors on an anisotropic lattice: Light-hadron spectroscopy and setting the strange-quark mass

Huey-Wen Lin,[1,*] Saul D. Cohen,[1] Jozef Dudek,[1] Robert G. Edwards,[1] Bálint Joó,[1] David G. Richards,[1] John Bulava,[2] Justin Foley,[2] Colin Morningstar,[2] Eric Engelson,[3] Stephen Wallace,[3] K. Jimmy Juge,[4] Nilmani Mathur,[5] Michael J. Peardon,[6] and Sinéad M. Ryan[6]

(Hadron Spectrum Collaboration)

[1]*Thomas Jefferson National Accelerator Facility, Newport News, Virginia 23606, USA*
[2]*Department of Physics, Carnegie Mellon University, Pittsburgh, Pennsylvania 15213, USA*
[3]*Department of Physics, University of Maryland, College Park, Maryland 20742, USA*
[4]*Department of Physics, University of the Pacific, Stockton, California 95211, USA*
[5]*Department of Theoretical Physics, Tata Institute of Fundamental Research, Mumbai 400005, India*
[6]*School of Mathematics, Trinity College, Dublin 2, Ireland*
(Received 24 November 2008; published 3 February 2009)

We present the first light-hadron spectroscopy on a set of $N_f = 2 + 1$ dynamical, anisotropic lattices. A convenient set of coordinates that parameterize the two-dimensional plane of light and strange-quark masses is introduced. These coordinates are used to extrapolate data obtained at the simulated values of the quark masses to the physical light and strange-quark point. A measurement of the Sommer scale on these ensembles is made, and the performance of the hybrid Monte Carlo algorithm used for generating the ensembles is estimated.

DOI: 10.1103/PhysRevD.79.034502 PACS numbers: 11.15.Ha, 12.38.Gc, 12.38.Lg

I. INTRODUCTION

Understanding the internal structure of nucleons has been a central research topic in nuclear and particle physics for many decades. As detailed experimental data continue to emerge, improved theoretical understanding of the hadronic spectrum will be needed to learn more about the complex, confining dynamics of quantum chromodynamics (QCD). Lattice calculations offer a means of linking experimental data to the Lagrangian of QCD, allowing access to the internal structure of any resonance.

At Jefferson Laboratory (JLab), an ambitious program of research into a range of hadronic excitations is underway. To date, the Hall B experiment has collected a large amount of data regarding the spectrum of excitations of the nucleons. The Excited Baryon Analysis Center (EBAC) [1,2] aims to review all observed nucleon excitations systematically and to extract reliable parameters describing transitions between resonances and the ground-state nucleons. The 12-GeV upgrade of JLab's CEBAF accelerator will make possible the GlueX experiment, which will produce an unprecedented meson dataset through photoproduction. A particular focus will be the spectrum of hadrons with exotic quantum numbers, which can arise when the gluonic field within a meson carries nonvacuum quantum numbers. Such ''hybrid'' mesons offer a window into the confinement mechanism and will be studied theoretically in some detail using lattice methods. Lattice spectroscopy can determine the properties of isoscalar mesons as well, including any possible candidate glueballs.

Accurate resolution of excited states using lattice QCD has proven difficult. In Euclidean space, excited-state correlation functions decay faster than the ground state and at large times are swamped by the larger signals of lower states. To improve the chances of extracting excited states, better temporal resolution of correlation functions is extremely helpful. An anisotropic lattice, where the temporal domain is discretized with a finer grid spacing than its spatial counterpart, is one means of providing this resolution while avoiding the increase in computational cost that would come from reducing the spacing in all directions. This finer resolution must be combined with application of variational techniques to construct operators that overlap predominantly with excited states. In a series of papers [3–7], techniques to construct operators in irreducible representations of the cubic group to extract radially and orbitally excited states were presented. Application of these techniques to quenched anisotropic lattices shows clear signals as high as the eighth excited state. Also possible on the anisotropic lattice are studies of radiative transitions in meson systems [8] and nucleon-P_{11} transition form factors [9].

Making the lattice discretization anisotropic comes with a price, however. Since hypercubic symmetry is broken down to just the cubic group, relevant (dimension-four) operators can mix in the lattice action. To ensure the continuum limit of the lattice theory has full Lorentz invariance, a nonperturbative determination of the lattice

*hwlin@jlab.org

action parameters that enforce the symmetry at finite lattice spacing in some low-energy observables has been performed [10]. In work to be reported elsewhere, a perturbative determination of these action parameters is also being carried out by this collaboration [11].

In this study, we perform three-flavor dynamical calculations with two degenerate light quarks and a strange quark. In a previous study, we tuned a three-flavor lattice action to ensure Lorentz symmetry is restored in appropriately chosen low-energy observables. We showed empirically that restoring the symmetry at quark masses below 175 MeV requires only small changes to the action parameters, and no further determinations of these parameters is needed within the scope of this study. Our fermion action is a Sheikholeslami-Wohlert discretization, generalized to the anisotropic lattice [12]. The fermion fields interact with the gluons via three-dimensionally stout-smeared [13] links, and the gluon action is Symanzik improved at the tree level of perturbation theory. To assess the cost of these dynamical calculations, we study the efficiency of the hybrid Monte Carlo (HMC) algorithm in large-scale production simulations.

Using current algorithms and computing resources, it remains impractical to run calculations at the physical value of the light-quark mass. An extrapolation of the light-quark dependence of simulation data is needed. While simulations straddling the correct strange-quark mass have been performed, determining the appropriate choice of mass in the Lagrangian is also problematic; *a priori*, this value is not known and changing the bare strange-quark mass affects all lattice observables in a delicate way. This work proposes a simple means of setting the lattice strange-quark mass by examining dimensionless ratios with mild behavior in the light-quark chiral limit. A new set of coordinates, parameterizing the space of theories with different light and strange-quark masses is introduced to help this process. We use the ratios $l_\Omega = 9m_\pi^2/4m_\Omega^2$ and $s_\Omega = 9(2m_K^2 - m_\pi^2)/4m_\Omega^2$, inspired by expanding the pseudoscalar meson masses to leading order in chiral perturbation theory.

With this framework in place, the spectrum of some ground-state mesons and baryons is determined and extrapolated to the physical quark masses using leading-order chiral perturbation theory. The Sommer scale [14] is determined (in units of the Omega-baryon mass) on a subset of our ensembles and extrapolated to the physical quark masses. Using this method, we intend to continue our exploration of excited-state hadrons, including isoscalar and hybrid mesons. A clear means of handling unstable states is needed, and our suite of measurement technology is currently under further development. A study of these techniques on $N_f = 2$ dynamical lattices gives us confidence that more precise understanding of these states will be forthcoming.

The structure of this paper is as follows: In Sec. II, we will discuss the actions and algorithms used in this work, and the performance of the method used to generate Monte Carlo ensembles is examined. The details of the measurements we performed on these ensembles is presented in Sec. III. Section IV presents the method we propose to set the strange-quark mass, including the dimensionless coordinates used for extrapolating quantities measured at unphysical quark masses to the physical theory. Our determination of a selection of states in the hadron spectrum and the Sommer scale is given in Sec. V. Some conclusions and future outlook are presented in Sec. VI.

II. SIMULATION DETAILS

In this section details of the lattice action and the performance of the hybrid Monte Carlo algorithm are presented. Monte Carlo simulations were performed on lattices with grid spacings of a_s and a_t in the spatial and temporal directions, respectively, and with physical volumes $L_s^3 \times L_t$, where $L_s = N_s a_s$ and $L_t = N_t a_t$. Lattices with extents $N_s^3 \times N_t = 12^3 \times 96$, $16^3 \times 96$, $16^3 \times 128$ and $24^3 \times 128$ were employed.

A. Action

The gauge and fermion actions used in this work are described in great detail in our previous work [10]. For completeness in this paper, we briefly review the essential definitions. For more detailed definitions, see Ref. [10].

For the gauge sector, we use a Symanzik-improved action with tree-level tadpole-improved coefficients

$$S_G^\xi[U] = \frac{\beta}{N_c \gamma_g}\left\{\sum_{x,s\neq s'}\left[\frac{5}{6u_s^4}\Omega_{\mathcal{P}_{ss'}}(x) - \frac{1}{12u_s^6}\Omega_{\mathcal{R}_{ss'}}(x)\right] + \sum_{x,s}\gamma_g^2\left[\frac{4}{3u_s^2u_t^2}\Omega_{\mathcal{P}_{st}}(x) - \frac{1}{12u_s^4u_t^2}\Omega_{\mathcal{R}_{st}}(x)\right]\right\}, \tag{1}$$

where $\Omega_W = \mathrm{Re\,Tr}(1 - W)$ and $W = \mathcal{P}$, the plaquette, or $\mathcal{R}_{\mu\nu}$, the 2×1 rectangular Wilson loop (length two in the μ direction and one in the ν direction) with $\{s, s'\} \in \{x, y, z\}$. The parameter γ_g is the bare gauge anisotropy, $N_c = 3$ indicates the number of colors, β is related to the coupling g^2 through $\beta = 2N_c/g^2$, and u_s and u_t are the spatial and temporal tadpole factors. This action has leading discretization error at $O(a_s^4, a_t^2, g^2a_s^2)$ and possesses a positive-definite transfer matrix, since there is no length-two rectangle in time.

In the fermion sector, we adopt the anisotropic clover fermion action [12]

$$S_F^\xi[U, \bar\psi, \psi] = \sum_x \bar{\hat\psi}(x)\frac{1}{\tilde u_t}\left\{\tilde u_t\hat m_0 + \gamma_t\hat W_t + \frac{1}{\gamma_f}\sum_s\gamma_s\hat W_s - \frac{1}{2}\left[\frac{1}{2}\left(\frac{\gamma_g}{\gamma_f} + \frac{1}{\xi_R}\right)\frac{1}{\tilde u_t\tilde u_s^2}\sum_s\sigma_{\mathrm{ts}}\hat F_{\mathrm{ts}} + \frac{1}{\gamma_f}\frac{1}{\tilde u_s^3}\sum_{s<s'}\sigma_{ss'}\hat F_{ss'}\right]\right\}\hat\psi(x), \tag{2}$$

where γ_f is the bare fermion anisotropy and $\xi_R = a_s/a_t$ is the renormalized anisotropy. $\gamma_{s,t}$, σ_{st} and $\sigma_{ss'}$ (with $\sigma_{\mu\nu} = [\gamma_\mu, \gamma_\nu]/2$) are Dirac matrices. Hats denote dimensionless variables that connect to dimensionful quantities as quark field $\hat{\psi} = a_s^{3/2}\psi$, bare quark mass $\hat{m}_0 = m_0 a_t$, gauge field strength $\hat{F}_{\mu\nu} = a_\mu a_\nu F_{\mu\nu} = \mathrm{Im}(\mathcal{P}_{\mu\nu}(x))/4$ and "Wilson operator" $\hat{W}_\mu \equiv \hat{\nabla}_\mu - \gamma_\mu \hat{\Delta}_\mu/2$ (with $\hat{\nabla}_\mu = a_\mu \nabla_\mu$, $\hat{\Delta}_\mu = a_\mu^2 \Delta_\mu$). The gauge links in the fermion action are three-dimensionally stout-link smeared gauge fields with smearing weight $\rho = 0.14$ and $n_\rho = 2$ iterations. $\tilde{u}_s$ and $\tilde{u}_t$ are the spatial and temporal tadpole factors from smeared fields, respectively.

In our previous work [10], we found at $\beta = 1.5$, that the tadpole factors are

$$u_s = 0.7336,\ u_t = 1, \qquad \tilde{u}_s = 0.9267,\ \tilde{u}_t = 1. \tag{3}$$

Tuning the anisotropy for all quark masses (even below the chiral limit) gives the desired $\gamma^*_{g,f}$

$$\gamma^*_g = 4.3, \qquad \gamma^*_f = 3.4. \tag{4}$$

B. Algorithm

We use the rational hybrid Monte Carlo (RHMC) algorithm for gauge generation [15]. The theoretical aspects of our procedure were discussed in detail in Ref. [10]. Here, we discuss only the aspects that are specific to the calculations presented in this work.

We use rational approximations for both the light-quark fields and for the strange quarks—one field for each light-quark flavor and another one for the strange. We employ even-odd preconditioning for the Wilson clover operator, obtaining the Hamiltonian

$$\begin{aligned} H = &\frac{1}{2}\sum_{x,\mu} \mathrm{Tr}\pi^\dagger \pi - 2\sum_x \mathrm{Tr}\log A_{ee}(m_l) \\ &- \sum_x \mathrm{Tr}\log A_{ee}(m_s) + S_F(m_l) + S_F(m_l) \\ &+ S_F(m_s) - S^s_G - S^t_G, \end{aligned} \tag{5}$$

where π are the momenta conjugate to the gauge fields; terms involving A_{ee} contribute effects due to the parts of the preconditioned clover determinant coming from the submatrix connecting even sites; S^s_G and S^t_G are the parts of the gauge action involving loops in the spatial directions only and with loops including time direction, respectively; and $S_F(m_l)$ and $S_F(m_s)$ are pseudofermion terms for the rational approximations to the fermion action corresponding to the light- and strange-quark fields, respectively, which we discuss below.

The pseudofermion terms $S_F(m)$ employ a rational approximation to the fermion determinant of the even-odd preconditioned clover operator coming from the submatrix connecting the odd sites for a quark with mass m. This submatrix is

$$M(m;\tilde{U}) = A_{oo}(m;\tilde{U}) - D_{oe}(\tilde{U})A^{-1}_{ee}(m;\tilde{U})D_{eo}(\tilde{U}), \tag{6}$$

where A_{oo} is the clover operator on the odd sites, A^{-1}_{ee} is the inverse clover operator on the even sites, and $D_{oe}(D_{eo})$ is the Wilson hopping term connecting odd sites with even (even sites with odd). In all the expressions, $\tilde{U}$ denotes stout-smeared gauge fields U, which were smeared as described in Sec. II A.

To construct our pseudofermion actions, we use the rational approximation $R^{a/b}(M^\dagger M)$ in partial-fraction form:

$$R^{a/b}(M^\dagger M) = \alpha \sum_i p_i (M^\dagger M + q_i)^{-1} \approx (M^\dagger M)^{a/b}, \tag{7}$$

where we drop the quark-mass dependence of M for clarity. The coefficients α, p_i, and q_i define the approximation and are determined via the Remez algorithm [16,17] applied over the spectral bounds of the operator $M^\dagger M$. In particular, we needed to compute approximations with $(a, b) = (-1, 4)$ for evaluating the actions (see below), $(a, b) = (1, 4)$ for pseudofermion refreshment and $(a, b) = (-1, 2)$ for our molecular dynamics (MD). Our approximation bounds for the action are shown in Table I. We solve the linear system resulting from applying $R^{a/b}$ to pseudofermion fields using the multishift conjugate gradient algorithm [18]. We use a stopping relative residuum $r < 10^{-8}$ in our energy calculations, where the residuum for pole i is

$$r_i = \frac{||\phi - (M^\dagger M + q_i)\psi_i||}{||\phi||}, \tag{8}$$

where ϕ is the pseudofermion field and ψ_i is the solution corresponding to the i-th pole. However, since the multishift algorithm cannot be restarted, our stopping was based on estimates of r_i accumulated with the short-term recurrence in the solver algorithm, which may be slightly different from the true residual as defined in Eq. (8) due to solver stagnation and rounding effects. To minimize rounding effects we accumulated sums and inner products using double precision.

TABLE I. Details of the approximations used for the pseudofermionic action $R^{-(1/4)}$. We show the bounds, the number of poles, and the maximum error for the approximation to the light and strange pseudofermion terms.

V	Light quark				Strange quark			
	$a_t m_l$	Bounds	No. poles	Max. error	$a_t m_s$	Bounds	No. poles	Max. error
$24^3 \times 128$	-0.0840	$(5 \times 10^{-6}, 10)$	16	1.8×10^{-8}	-0.0743	$(10^{-4}, 10)$	12	8.8×10^{-8}

TABLE II. Details of the approximations used for the force $R^{-(1/2)}$. We show the bounds, the number of poles, and the maximum error for the approximation to the light and strange pseudofermion terms.

V	Light quark				Strange quark			
	$a_t m_l$	Bounds	No. poles	Max. error	$a_t m_s$	Bounds	No. poles	Max. error
$24^3 \times 128$	-0.0840	$(5 \times 10^{-6}, 10)$	12	2.5×10^{-6}	-0.0743	$10^{-4}, 10)$	10	2.0×10^{-6}

Our pseudofermion action terms are

$$S_F = X^\dagger X, \qquad X = R^{-(1/4)}(M^\dagger M)\phi = \alpha \sum_i p_i \psi_i, \quad (9)$$

individually for each flavor. We do not need to employ multiple pseudofermion fields per flavor in this study.

During our simulation, we adjusted our approximation range by measuring eigenvalue bounds every five trajectories during the process of thermalization. Thereafter, we continued to measure the bounds to ensure we do not suffer from boundary violations.

Our molecular dynamics process employs a rational force

$$F = -\alpha \sum_i p_i \psi_i^\dagger \left(\frac{dM^\dagger}{dU} M + M^\dagger \frac{dM}{dU} \right) \psi_i, \quad (10)$$

where i runs over the number of poles in the approximation $R^{-(1/2)}$. Time derivatives are evaluated over the stouted gauge field $\tilde{U}$, and only the final sum is recursed down to compute the force for the thin links U.

We employ a multiple-timescale integration scheme for the molecular dynamics evolution [19] by nesting a second-order Omelyan [20,21] integration step at each timescale. Our largest forces come from the temporal directions: the gauge force from S_G^t and the temporal forces generated by the pseudofermions. To mitigate the numerical effort needed [22], we place the S_G^t term in the action on a finer timescale than the other terms, and to deal with the temporal forces from the pseudofermion terms, employ an anisotropic timestep with temporal timestep dt of length

$$dt_t = dt_s / \xi_{\mathrm{MD}}, \quad (11)$$

where $\xi_{\mathrm{MD}} = 3.5$. Apart from the above, we find the forces from S_G^s and the spatial forces from the S_F terms to be within a factor of 2 of each other, so we place them on the same timescale. The forces from the $\mathrm{Tr}\log A_{ee}$ terms are very small in comparison but have small numerical cost, so we place them on the same timescale as S_G^s and S_F.

We note that the Hamiltonian for the MD does not need to be known as accurately as the one for the energy calculations; all that is required is for the MD to be reversible, area-preserving, and (as a practical matter) for the acceptance rate to be reasonable. To save on numerical effort we solved our systems of linear equations only to a residuum r_{MD} of at most $r_{\mathrm{MD}} < 10^{-6}$. Correspondingly, we never required the rational approximation to $R^{-(1/2)}$ to have a maximum error better than 10^{-6}, resulting in a smaller number of poles in the approximation than we need for the energy calculations. Further, to make the MD even less numerically intensive, we follow Refs. [23,24] by relaxing the requirements on the residua for individual poles in $R^{-(1/2)}$. We use a range of $r_{\mathrm{MD}} < 10^{-4}$ for the smallest shifts and $r_{\mathrm{MD}} < 10^{-6}$ for the larger shifts. We tune our molecular dynamics to attain an overall acceptance rate close to 70%. We show in Table II the bounds of the MD rational approximation used for the run with $V = 24^3 \times 128$, $(a_t m_l, a_t m_s) = (-0.0840, -0.0743)$. We show the residua requested in the MD evolution in Table III, and the timesteps and the resulting acceptance rate in Table IV.

C. Thermalization and autocorrelation

During the first segment of each gauge ensemble generation, some special conditions apply. We do not apply the acceptance test during the first $O(10)$ trajectories in each series, which allows a fast initial approach to the vicinity of the equilibrium. Such a scheme is particularly important in the case of simulations starting from totally ordered or disordered configurations. Wherever possible, however, we begin the algorithm with an equilibrated configuration from a simulation at nearby parameters. Also, during this phase (as mentioned above), the minimum and maximum eigenvalue bounds are updated every 5 trajectories.

TABLE III. Requested residua for the poles in the MD force approximation from the smallest shifts (leftmost) to larger shifts (rightmost).

V	$(a_t m_l, a_t m_s)$	Poles for $a_t m_l$	Residua	Poles for $a_t m_s$	Residua
$24^3 \times 128$	$(-0.0840, -0.0743)$	12	$10^{-4}, 10^{-4}, 5 \times 10^{-5}, 5 \times 10^{-5}, 5 \times 10^{-5}, 10^{-5}, 10^{-5}, 5 \times 10^{-6}, 5 \times 10^{-6}, 5 \times 10^{-6}, 3 \times 10^{-6}, 10^{-6}$	10	$10^{-4}, 10^{-4}, 5 \times 10^{-5}, 10^{-5}, 10^{-5}, 10^{-5}, 5 \times 10^{-6}, 5 \times 10^{-6}, 3 \times 10^{-6}, 10^{-6}$

TABLE IV. The two timescales used in the molecular dynamics integration. The spatial timestep for the coarse scale is dt_s^1, and for the finer scale it is dt_s^2, which we display as a fraction of dt_s^1 here. We also show our MD timestep anisotropy. On each scale, $dt_t^i = dt_s^i/\xi_{\mathrm{MD}}$. Finally, we show the average acceptance rate for the molecular dynamics with these step sizes.

V	$(a_t m_l, a_t m_s)$	dt_s^1	dt_s^2/dt_s^1	ξ_{MD}	Acceptance rate
$24^3 \times 128$	$(-0.0840, -0.0743)$	$\frac{1}{16}$	$\frac{1}{4}$	3.5	0.71

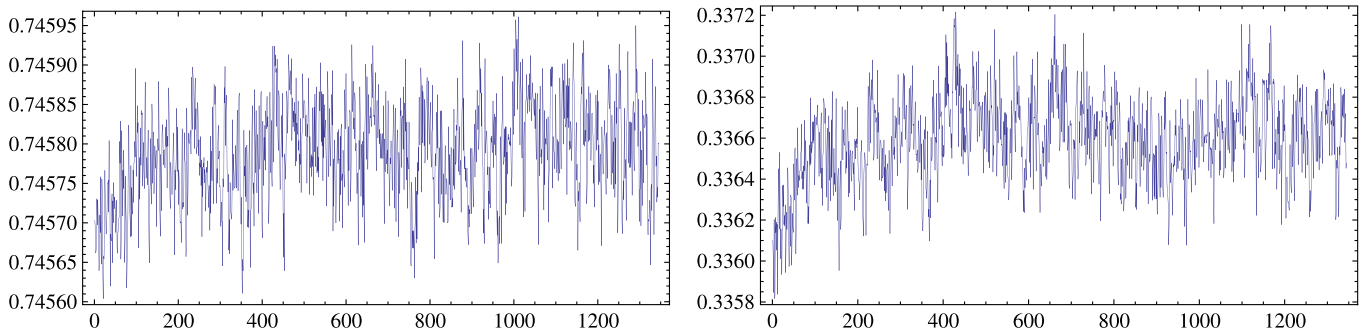

FIG. 1 (color online). Temporal (left column) and spatial (right column) plaquette history from the ensemble with $24^3 \times 128$ volume and $a_t m_l = -0.0840$. The x axis is in units of trajectories.

Figure 1 shows its plaquette history for $24^3 \times 128$ volume and $a_t m_l = -0.0840$. Both plaquette histories (one excluding temporal links and the other including only plaquettes with temporal links) show that equilibrium is reached long before 1000 RHMC trajectories. Therefore, to allow for thermalization of our gauge ensembles during the RHMC, we discard the initial 1000 trajectories from each set.

Figure 2 shows a histogram of the lowest eigenvalues of the Dirac operator $M^\dagger M$ for the light and strange quarks from the ensemble with $24^3 \times 128$ volume and $a_t m_l = -0.0840$. The lowest eigenvalues remain safely above the minimum eigenvalue bounds in which our rational approximation is valid. In addition, they show a clear gap away from zero, where the stability of the algorithm might be compromised.

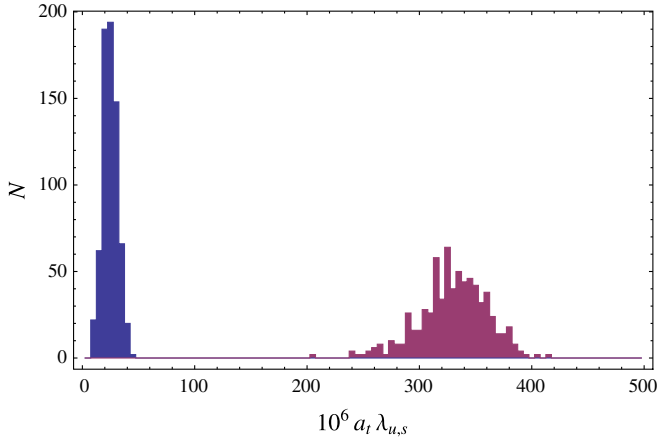

FIG. 2 (color online). Histogram of the lowest eigenvalues of the Dirac operator for the light and strange quarks from the ensemble with $24^3 \times 128$ volume and $a_t m_l = -0.0840$. The minimum values of the eigenvalues are $a_t \lambda = 6.9 \times 10^{-6}$ and 2.0×10^{-4} for the light and strange quarks, respectively.

The autocorrelation function is defined as

$$\rho(t) = \langle (\mathcal{O}(t') - \langle \mathcal{O} \rangle)(\mathcal{O}(t'+t) - \langle \mathcal{O} \rangle) \rangle, \qquad (12)$$

where $\langle \ldots \rangle$ means taking an average over the samples, t is the trajectory difference in the autocorrelation (from 1 to N total trajectories), and different t' (also indexing trajectory number) are averaged. To calculate the integrated autocorrelation length τ_{int} with a jackknife-estimated errorbar, we first divide the configurations into blocks of size N_b; we calculate $\rho_j(t)$ for the jackknife index j by ignoring contributions when either t or $t' + t$ is located within the j-th block and replacing $\langle \mathcal{O} \rangle$ by $\langle \mathcal{O} \rangle_j$, the mean value without the j-th block. With a jackknife dataset of length N/N_b, we calculate integrated autocorrelation length

$$\tau_{\mathrm{int}}(t_{\mathrm{max}}) = \frac{1}{2} + \frac{1}{\rho(t=0)} \sum_{t=1}^{t_{\mathrm{max}}} \rho(t), \qquad (13)$$

using the standard jackknife procedure. The autocorrelations of the spatial plaquette from gauge ensemble $a_t m_l = -0.0808$, $16^3 \times 128$ are shown in Fig. 3; the integrated autocorrelation length for the stout-smeared plaquette is about 30 trajectories, which is around twice as large as the unsmeared ones. The integrated autocorrelation length for lowest light and strange eigenvalues are around 13 and 10 trajectories, respectively, as shown in Fig. 4. Figure 5 shows the case of pion and proton correlators at $t = 30$ on our largest spectrum measurement (518 configurations)

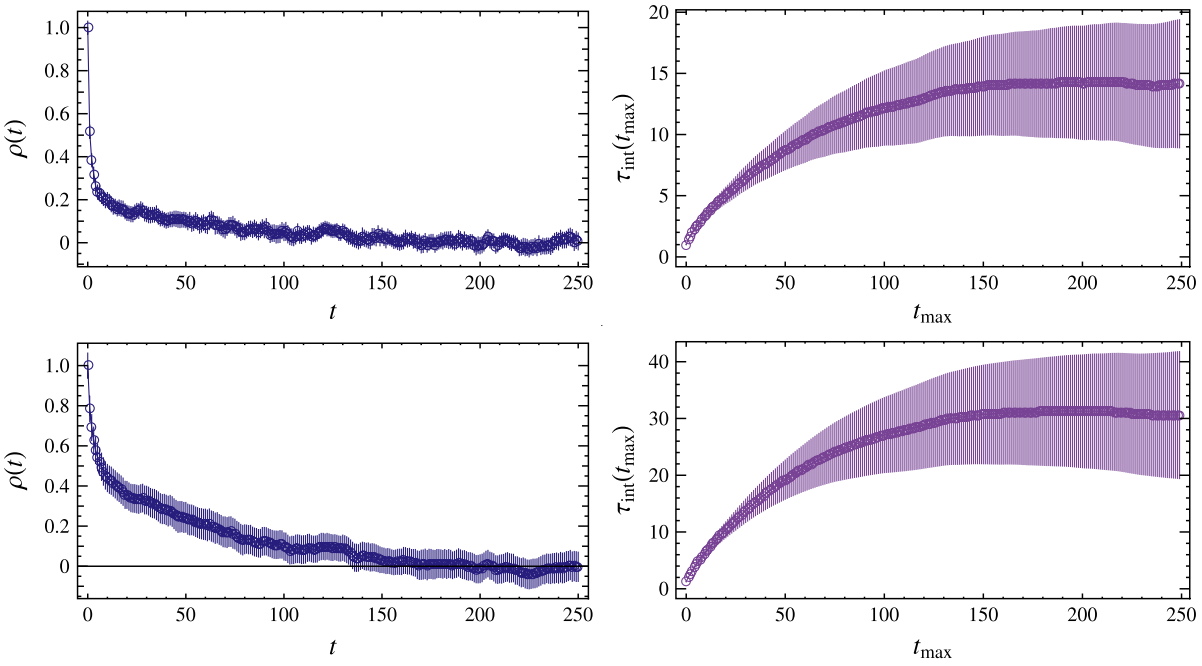

FIG. 3 (color online). Autocorrelation $\rho(t)$ and integrated autocorrelation length τ_{int} (in trajectories) for the unsmeared (above) and smeared (below) plaquette involving only spatial links from the ensemble with $16^3 \times 128$ volume and $a_t m_l = -0.0808$.

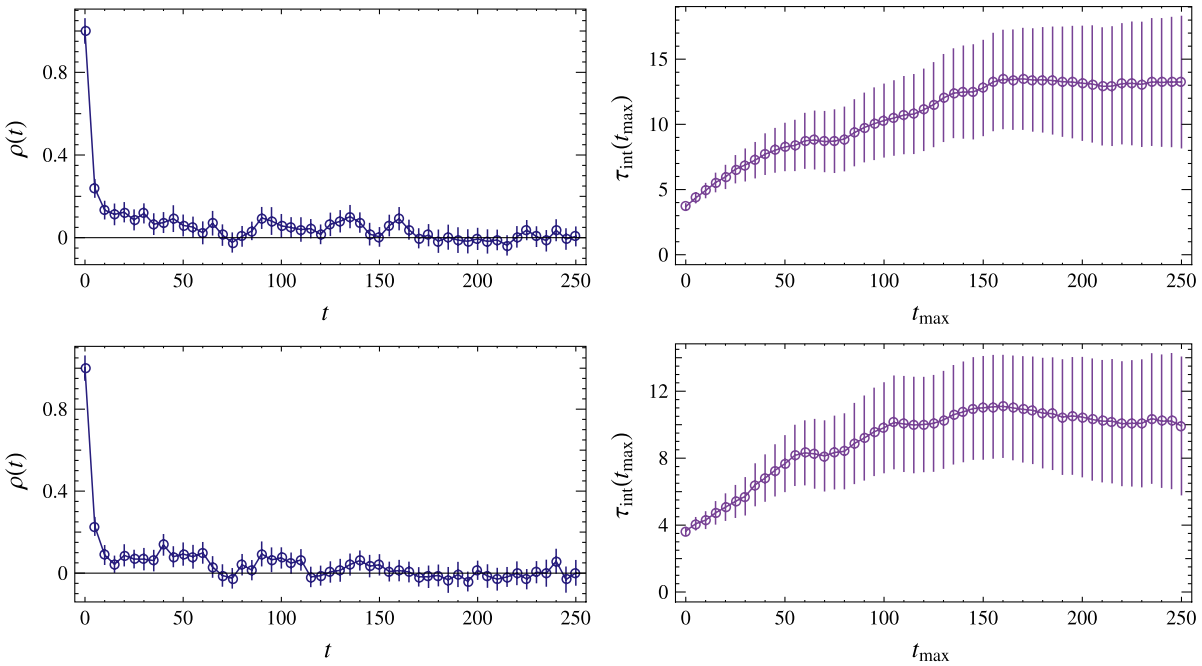

FIG. 4 (color online). Autocorrelation $\rho(t)$ and integrated autocorrelation length τ_{int} (in trajectories) for the up/down (above) and strange (below) quark eigenvalues from the ensemble with $16^3 \times 128$ volume and $a_t m_l = -0.0808$.

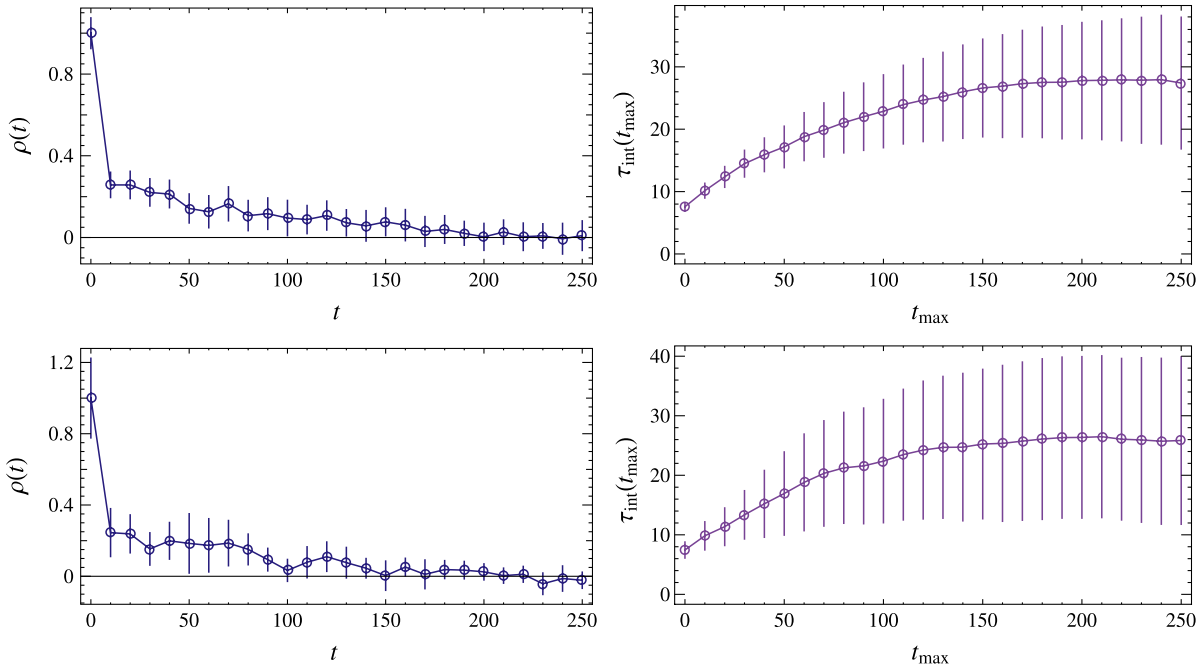

FIG. 5 (color online). Autocorrelation $\rho(t)$ and integrated autocorrelation length τ_{int} (in trajectories) for the pion (above) and proton (below) correlator at $t = 30$ from the ensemble with $16^3 \times 128$ volume and $a_t m_l = -0.0808$.

ensemble, $a_t m_l = -0.0808$, $16^3 \times 128$. The integrated autocorrelation length is about 30 trajectories.

III. MEASUREMENT TECHNIQUES

In this section, the methods used to determine relevant spectroscopy data on the Monte Carlo ensembles are described. We have used well-established lattice spectroscopy technology throughout this calculation.

To better access ground-state correlation functions, we use the variational method [25,26]. Consider the generalized eigenvalue problem

$$C(t)v = \lambda(t, t_0)C(t_0)v, \tag{14}$$

where t_0 is chosen as the earliest time at which our model (given below) well describes the correlator C. $C_{ij}(t)$ is a two-point correlation function, composed from the operators $\mathcal{O}_i$ and $\mathcal{O}_j$. The correlation matrix can be approximated by a sum over the lowest N states:

$$C_{ij}(t) = \sum_{n=1}^{\infty} z_{ni}{}^* z_{nj} e^{-E_n(t-t_0)}, \tag{15}$$

$$\approx \sum_{n=1}^{N} u_{ni}{}^* u_{nj} e^{-E_n(t-t_0)}, \tag{16}$$

where E_n is the energy of the n-th state, and $u_m \cdot z_n = \delta_{mn}$. We extract the energies from the eigenvalues

$$\lambda_n(t, t_0) = e^{-E_n(t-t_0)}, \tag{17}$$

which are obtained by solving

$$C(t_0)^{-1/2}C(t)C(t_0)^{-1/2}v_n = \lambda_n(t, t_0)v_n. \tag{18}$$

A. Hadron correlation functions

We perform measurements starting from trajectory 1000 on every 10th trajectory, using the EigCG inverter (developed by A. Stathopoulos *et al.* in Ref. [27]) to calculate quark propagators (with CG residual set to 10^{-8}). We use four sources on each configuration, where a random source location is selected for the first source, and the remaining three are uniformly shifted by $N_{x,y,z}/2$ and $N_t/4$; this arrangement should reduce potential autocorrelations between configurations. We bin the data over spans of five measurements.

In this work, we construct a 3×3 correlator matrix C_{ij} by using three different Gaussian smearing widths ($\sigma \in \{3.0, 5.0, 6.5\}$) on the hadron operators. We extract the ground-state principal correlator and fit the ground-state mass using a cosh form. (We also try an exponential form on the principal correlator, and the fit results are consistent.) The t_{min} dependences (with $t_{\mathrm{max}} \approx 50$) of the fitted masses are shown in Fig. 6 for the pion, rho, nucleon, and Delta. The fitted masses are very consistent between various choices of starting time in the fits.

We use meson interpolating fields of the form $\bar{q}\Gamma q$, which overlap with the physical states listed in Table V; charge conjugation C applies only to particles with zero net flavor. The estimated η mass is $\sqrt{m_\pi^2/3 + 2m_{s\bar{s}}^2/3}$. The ground-state masses are summarized in Table VI. We have two volumes (12^3 and 16^3) of the lightest ensemble, $m_s = -0.0540$, and two (16^3 and 24^3) on $a_t m_s = -0.0743$: no major finite-volume effects are observed,

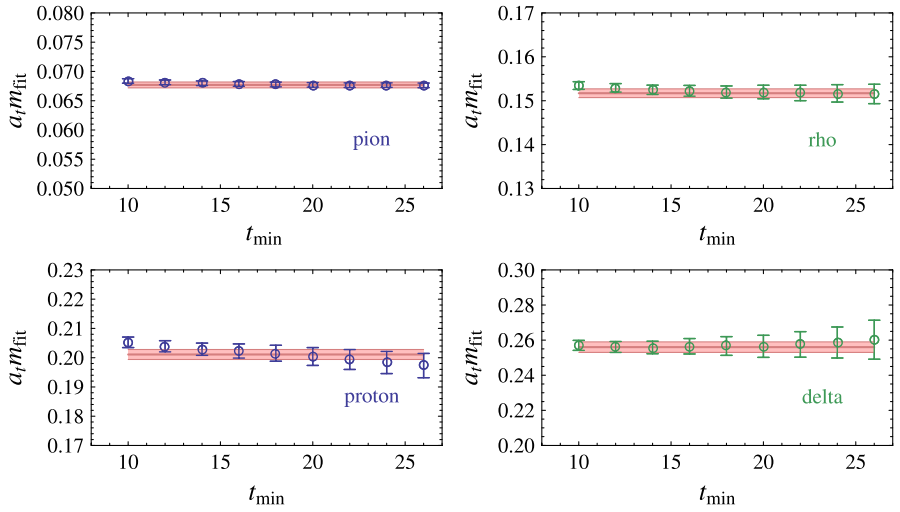

FIG. 6 (color online). Pion and rho (above) and proton and Delta (below) fitted masses as functions of $t_{\rm min}$, where $t_{\rm source}$ has been shifted to $t = 0$. The bands indicated the final fitted masses summarized in Tables VI and VII.

except for the a_0 mass from the $a_t m_s = -0.0743$ ensemble and baryon states from $a_t m_s = -0.0540$.

The octet baryons are calculated using the interpolating field $(q_1 C\gamma_4\gamma_5 q_2)q_1$ (with $q_i = u/d$ or s quark); the Λ uses $2(uC\gamma_5 d)s + (sC\gamma_5 d)u + (uC\gamma_5 s)d$; and the decuplet uses $2(q_2 C(1/2)(1+\gamma_4)\gamma_- q_1)q_1 + (q_1 C(1/2)\times(1+\gamma_4)\gamma_- q_1)q_2$ (with $\gamma_- = \gamma_x - \gamma_y$). The calculated octet and decuplet ground-state masses are summarized in Table VII. We observe a finite-volume discrepancy in the baryon sector on the lightest ensemble, $a_t m_s = -0.0540$. When we extrapolate the hadron masses to the physical limit, we will exclude the small volume sets: 12^3 with $a_t m_s = -0.0540$ and 16^3 with $a_t m_s = -0.0743$. Figures 7 and 8 show the squared-pion-mass dependence of these quantities. We note that for nonstrange hadrons, the sea strange-quark dependences are relatively mild.

At low pion masses, not all the states we calculate on the lattice are safe from decay. To check which particles may decay, we compare the particle masses to the threshold two-particle energies in each channel. The vector mesons could decay to two pseudoscalars in a P wave: $\rho \to \pi(p) + \pi(-p)$, $K^* \to K(p) + \pi(-p)$, and $\phi \to K(p) + \bar{K}(-p)$, where the minimum allowed momentum p on the lattice is $\frac{2\pi}{L_s}$. In Fig. 7, we plot the lowest two-particle energy threshold for the $m_s = -0.0540$ data with our two lattice extents (dot-dashed line) and $a_t m_s = -0.0743$ (dashed). All vector mesons in our calculation are well below threshold. The scalar mesons could decay to $\pi\eta$ in an S wave, which puts the states slightly below the

TABLE V. Meson interpolating operators. States are sorted into columns according to the degree of strangeness from 0 (left two columns) to 1 (right column) and then according to total isospin.

J^{PC}	Γ	$I=1$	$I=0$	$S=1$
0^{-+}	γ_5	π	$s\bar{s}$	K
1^{--}	γ_μ	ρ	ϕ	K^*
0^{++}	1	a_0		
1^{++}	$\gamma_\mu\gamma_5$	a_1		
1^{+-}	$\gamma_\mu\gamma_\nu$	b_1		

TABLE VI. Meson masses for $N_f = 3$ and $N_f = 2+1$ (in temporal lattice units).

N_s	N_t	$a_t m_l$	$a_t m_s$	$a_t m_\pi$	$a_t m_K$	$a_t m_\eta$	$a_t m_\rho$	$a_t m_{K^*}$	$a_t m_\phi$	$a_t m_{a_0}$	$a_t m_{a_1}$	$a_t m_{b_1}$	m_ρ/m_π	$N_{\rm cfg}$
12	96	−0.0540	−0.0540	0.2781(9)	0.2781(9)	0.2781(9)	0.334(3)	0.334(3)	0.334(3)	0.44(4)	0.474(15)	0.480(18)	0.833(7)	92
12	96	−0.0699	−0.0540	0.1992(17)	0.2227(15)	0.2450(13)	0.268(2)	0.2860(21)	0.3031(18)	0.37(2)	0.389(15)	0.377(13)	0.742(9)	110
12	96	−0.0794	−0.0540	0.1393(17)	0.1841(13)	0.2231(11)	0.201(7)	0.236(5)	0.268(3)	0.33(7)	0.317(14)	0.330(16)	0.69(2)	95
12	96	−0.0826	−0.0540	0.1144(19)	0.1691(17)	0.2142(15)	0.194(7)	0.232(4)	0.266(3)	0.22(4)	0.306(15)	0.266(19)	0.59(2)	84
16	96	−0.0826	−0.0540	0.113(3)	0.1669(15)	0.2112(15)	0.185(5)	0.222(4)	0.258(3)	0.28(4)	0.28(3)	0.28(2)	0.61(2)	25
12	96	−0.0618	−0.0618	0.2322(15)	0.2322(15)	0.2322(15)	0.286(5)	0.286(5)	0.286(5)	0.415(20)	0.436(15)	0.459(18)	0.812(12)	50
16	128	−0.0743	−0.0743	0.1483(2)	0.1483(2)	0.1483(2)	0.2159(6)	0.2159(6)	0.2159(6)	0.287(6)	0.317(5)	0.325(5)	0.6867(17)	79
16	128	−0.0808	−0.0743	0.0996(6)	0.1149(6)	0.1196(5)	0.173(2)	0.1819(21)	0.1901(18)	0.222(11)	0.252(6)	0.269(5)	0.574(6)	518
16	128	−0.0830	−0.0743	0.0797(6)	0.1032(5)	0.1100(4)	0.1623(16)	0.1733(10)	0.1845(11)	0.196(18)	0.236(8)	0.263(8)	0.491(6)	266
16	128	−0.0840	−0.0743	0.0691(6)	0.0970(5)	0.1047(5)	0.154(3)	0.1663(16)	0.1788(13)	0.159(15)	0.222(7)	0.238(8)	0.448(7)	224
24	128	−0.0840	−0.0743	0.0681(4)	0.0966(3)	0.1045(3)	0.1529(10)	0.1660(6)	0.1788(6)	0.194(14)	0.233(4)	0.242(6)	0.446(3)	287

TABLE VII. Baryon masses for $N_f = 3$ and $N_f = 2 + 1$ (in temporal lattice units).

N_s	N_t	$a_t m_l$	$a_t m_s$	$a_t m_\pi$	$a_t m_N$	$a_t m_\Sigma$	$a_t m_\Xi$	$a_t m_\Lambda$	$a_t m_\Delta$	$a_t m_{\Sigma^*}$	$a_t m_{\Xi^*}$	$a_t m_\Omega$	$N_{\rm cfg}$
12	96	−0.0540	−0.0540	0.2781(9)	0.521(4)	0.521(4)	0.521(4)	0.521(4)	0.556(7)	0.556(7)	0.556(7)	0.556(7)	92
12	96	−0.0699	−0.0540	0.1992(17)	0.398(5)	0.420(4)	0.439(4)	0.418(4)	0.452(6)	0.470(7)	0.487(6)	0.501(4)	110
12	96	−0.0794	−0.0540	0.1393(17)	0.318(6)	0.356(5)	0.386(4)	0.351(5)	0.365(10)	0.398(9)	0.424(7)	0.452(5)	95
12	96	−0.0826	−0.0540	0.1144(19)	0.295(11)	0.338(9)	0.369(6)	0.330(7)	0.353(10)	0.382(11)	0.414(8)	0.447(5)	84
16	96	−0.0826	−0.0540	0.113(3)	0.273(8)	0.316(7)	0.350(5)	0.310(6)	0.309(10)	0.347(9)	0.385(7)	0.423(8)	25
12	96	−0.0618	−0.0618	0.2322(15)	0.433(7)	0.433(7)	0.433(7)	0.433(7)	0.470(8)	0.470(8)	0.470(8)	0.470(8)	50
16	128	−0.0743	−0.0743	0.1483(2)	0.3165(18)	0.3165(18)	0.3165(18)	0.3165(18)	0.353(3)	0.353(3)	0.353(3)	0.353(3)	79
16	128	−0.0808	−0.0743	0.0996(6)	0.242(4)	0.259(4)	0.266(3)	0.256(3)	0.284(8)	0.297(6)	0.304(5)	0.311(6)	518
16	128	−0.0830	−0.0743	0.0797(6)	0.220(3)	0.242(3)	0.2510(19)	0.236(2)	0.270(7)	0.283(5)	0.292(4)	0.304(3)	266
16	128	−0.0840	−0.0743	0.0691(6)	0.207(4)	0.229(3)	0.239(2)	0.218(3)	0.262(8)	0.275(7)	0.282(5)	0.294(4)	224
24	128	−0.0840	−0.0743	0.0681(4)	0.2039(19)	0.2287(15)	0.2395(12)	0.2209(15)	0.256(3)	0.271(3)	0.282(2)	0.2945(16)	287

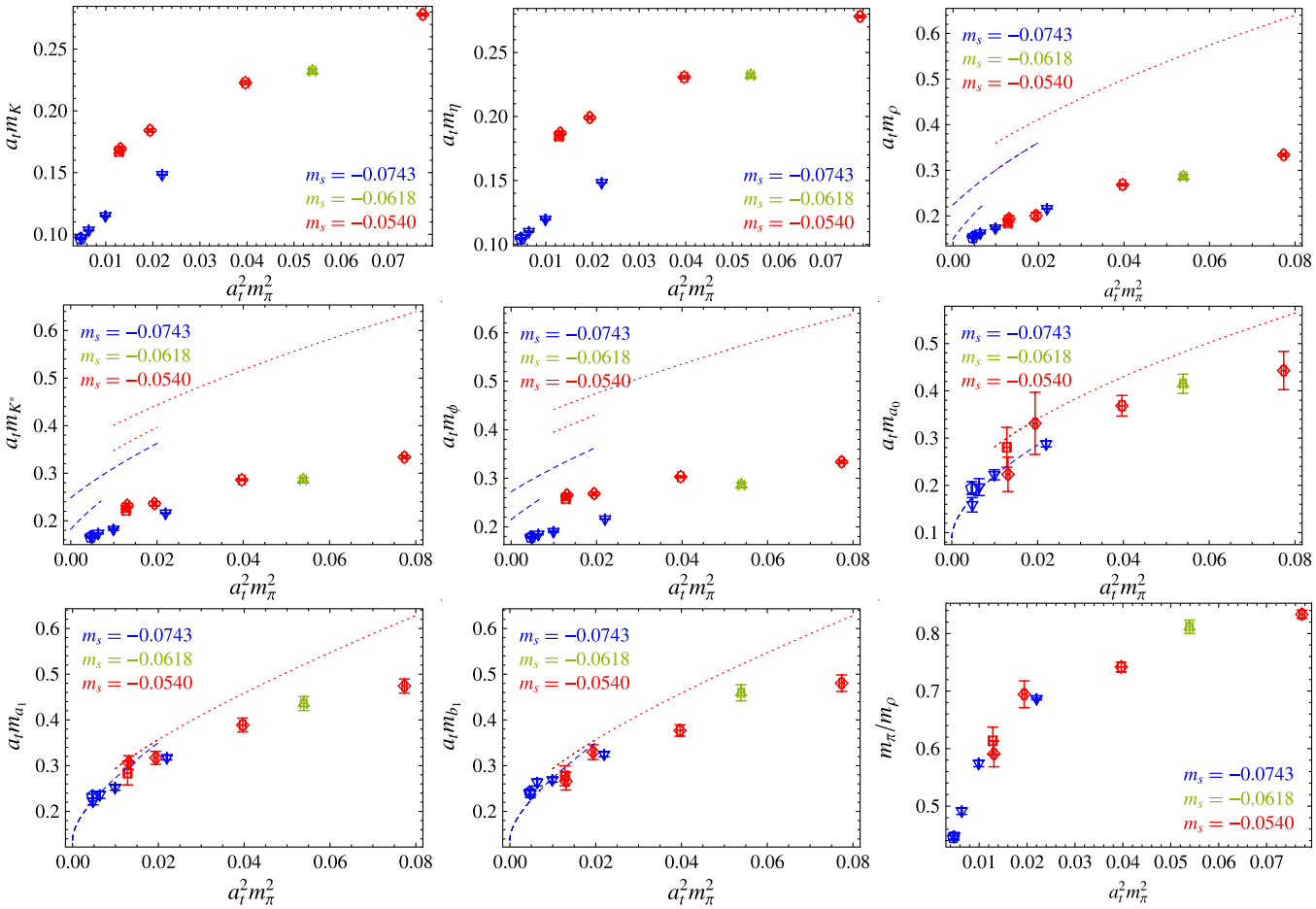

FIG. 7 (color online). All measured meson masses as functions of the squared pseudoscalar masses. The diamonds and squares are measured with $m_s = -0.0540$ but with two different volumes, $12^3 \times 96$ and $16^3 \times 96$; the upward-pointing triangles are those with $m_s = -0.0618$ and $12^3 \times 96$ volume; the downward triangles and pentagons are measured with $m_s = -0.0743$ and two different volumes, $16^3 \times 128$ and $24^3 \times 128$. The (red) dotted-dashed lines indicate the decay thresholds for the 12^3 (upper) and 16^3 (lower) $m_s = -0.0540$ ensembles, while the (blue) dashed lines are for the 16^3 (upper) and 24^3 (lower) $m_s = -0.0743$. The lowest decay thresholds are $\rho \to \pi(p) + \pi(-p)$, $K^* \to K(p) + \pi(-p)$, $\phi \to K(p) + \bar{K}(-p)$, $a_0 \to \pi(0) + \eta(0)$, $a_1 \to \pi(0) + \rho(0)$, and $b_1 \to \pi(0) + \omega(0)$ (with ω approximated by ρ), where the minimum allowed momentum p on the lattice is $\frac{2\pi}{L_s}$.

threshold. Similarly for the a_1 and b_1 mesons $a_1 \to \pi(0) + \rho(0)$ and $b_1 \to \pi(0) + \omega(0)$. In this case, we approximate the ω by the ρ, since their masses are similar. The a_0, a_1, and b_1 (especially for the $m_s = -0.0743$ ensemble) are slightly below the decay threshold. Fortunately, we have two volumes on the lightest m_l set; if these states are not single particle, the ratios of their overlap factors between the two volumes would be of order 2 or higher [28]. We find the ratios (using point-point correlators) to be 0.87 (12), 0.97(6), and 1.01(6), which indicates that our measurements are of single-particle states. The decuplet baryons are free from decays into an octet baryon. The lowest decay modes are $\Delta \to N(p) + \pi(-p)$, $\Sigma^* \to \Lambda(p) + \pi(-p)$, $\Xi^* \to \Xi(p) + \pi(-p)$, as shown in Fig. 8. Overall, most of the particles are stable.

TABLE VIII. Sommer scale r_0/a_s.

N_s	N_t	$a_t m_l$	$a_t m_s$	r_0/a_s
16	96	−0.0826	−0.0540	3.221(25)
12	96	−0.0794	−0.0540	3.110(31)
12	96	−0.0699	−0.0540	2.752(77)
12	96	−0.0540	−0.0540	2.511(14)
12	96	−0.0618	−0.0618	2.749(37)
16	128	−0.0840	−0.0743	3.646(10)
16	128	−0.0830	−0.0743	3.647(14)
16	128	−0.0808	−0.0743	3.511(12)
16	128	−0.0743	−0.0743	3.214(10)

Finally, we measure the renormalized fermion anisotropy on the $N_f = 2 + 1$ lattices. We tuned the fermion anisotropy in the three-flavor calculation in Ref. [10],

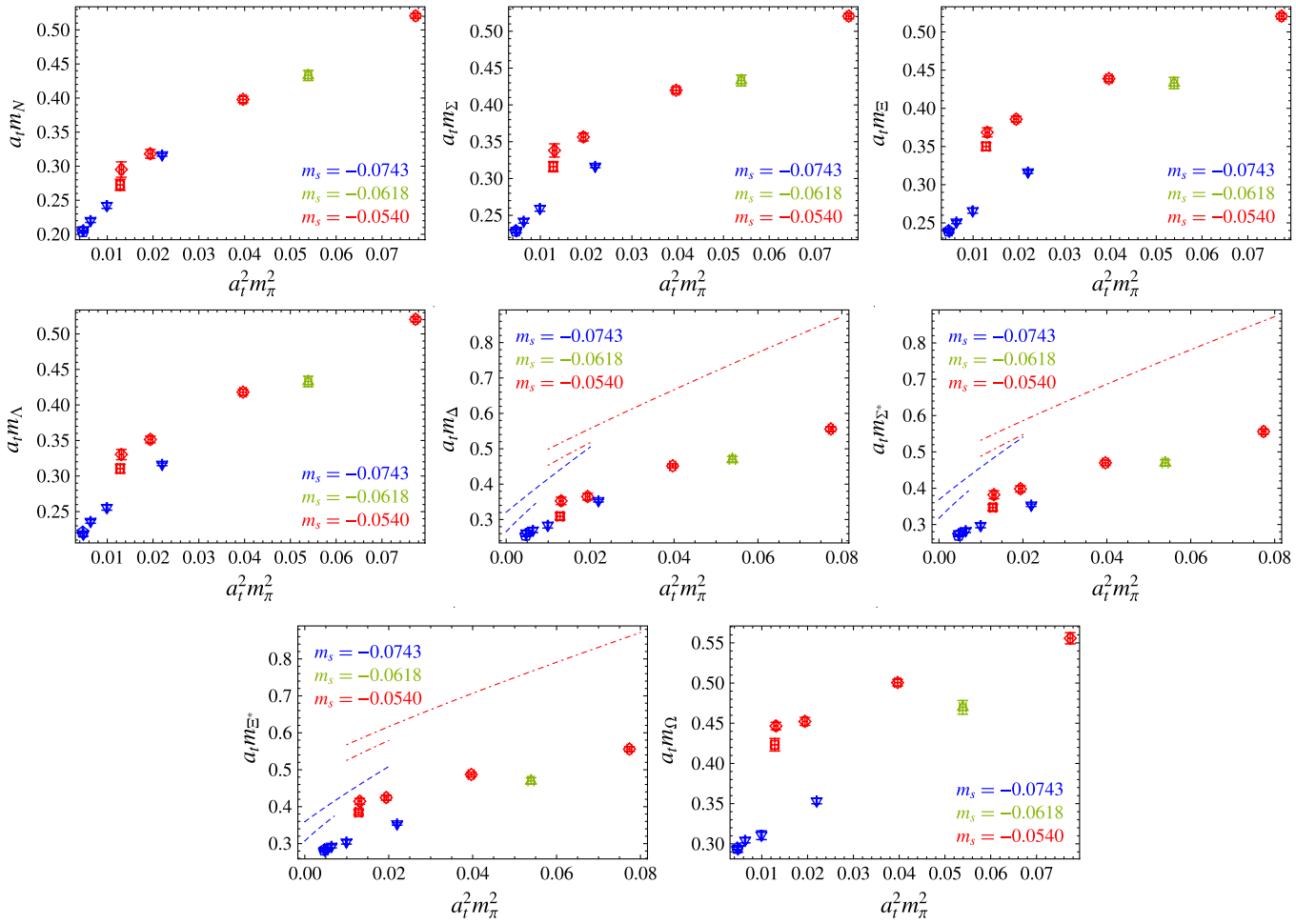

FIG. 8 (color online). All measured baryon masses as functions of the squared pseudoscalar masses. The diamonds and squares are measured with $m_s = -0.0540$ but with two different volumes, $12^3 \times 96$ and $16^3 \times 96$; the upward-pointing triangles are those with $m_s = -0.0618$ and $12^3 \times 96$ volume; the downward triangles and pentagons are measured with $m_s = -0.0743$ and two different volumes, $16^3 \times 128$ and $24^3 \times 128$. The (red) dotted-dashed lines indicate the decay thresholds for the 12^3 (upper) and 16^3 (lower) $m_s = -0.0540$ ensembles, while the (blue) dashed lines are for the 16^3 (upper) and 24^3 (lower) $m_s = -0.0743$. The lowest decay thresholds are $\Delta \to N(p) + \pi(-p)$, $\Sigma^* \to \Lambda(p) + \pi(-p)$, $\Xi^* \to \Xi(p) + \pi(-p)$, where the minimum allowed momentum p on the lattice is $\frac{2\pi}{L_s}$.

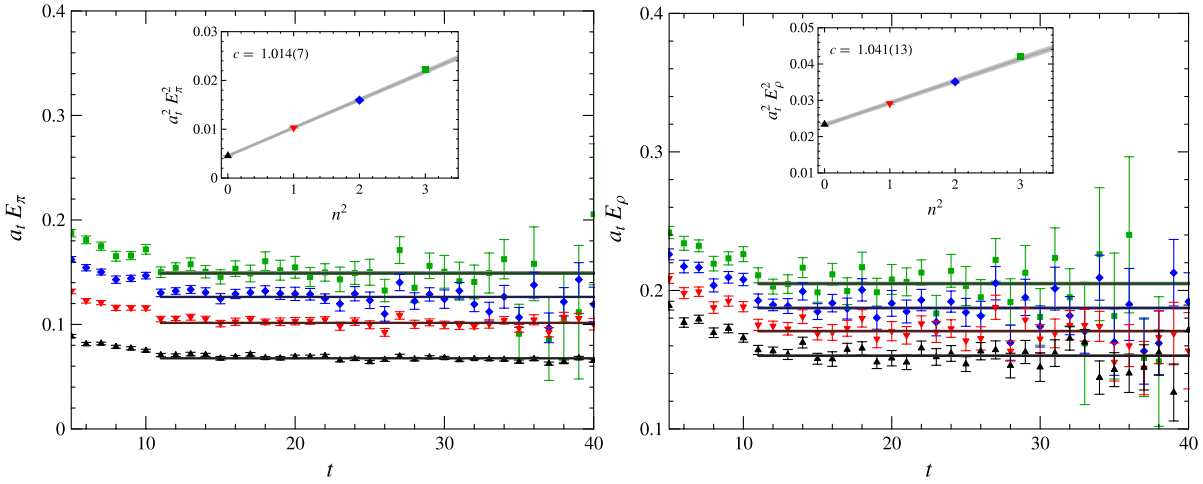

FIG. 9 (color online). Effective-mass plots using the ground-state principal correlators from the pion and rho-meson masses at four different momenta on the lightest ensemble ($m_s = -0.0743$) with volume $24^3 \times 128$. The insets show the energy squared in temporal lattice units versus n^2, which is related to the momentum by $p^2 = \frac{4\pi^2}{L_s^2} n^2$.

where we found that the fermion action coefficients are consistent for bare PCAC quark masses up to about 175 MeV. Figure 9 shows the meson dispersion on the $24^3 \times 128$, $a_t m_l = -0.0840$ and $a_t m_s = -0.0743$ ensembles. The effective mass plots are shown for the ground-state principal correlators at momenta $p = \frac{2\pi}{L_s} n$ with $n \in \{0, 1, 2, 3\}$; the fitted range and extracted energies are shown as straight lines across the effective mass plots. The inset shows the fitted renormalized fermion anisotropy at each n^2. The speed of light c is measured from the energy of the boosted hadron using $a_t^2 E_H(p)^2 = a_t^2 E_H(0)^2 + \frac{c^2}{\xi_R^2} \frac{4\pi^2}{N_s^2} n^2$. The values of c from the pion and rho mesons are about 2 and 3 standard deviations away from unity. Such a small deviation is also expected on isotropic lattices. For example, c for the pion and rho are about 2 standard deviations away from unity on the MILC coarse asqtad lattice ensembles [29].

B. Static-quark potential

$V(r)$, the energy of two static color sources separated by distance r provides a useful reference scale for spectrum calculations. This is most usefully described by the Sommer parameter r_0, defined by the condition

$$-\, r^2 \frac{\partial V(r)}{\partial r}\bigg|_{r=r_0} = 1.65. \tag{19}$$

The potential is computed by measuring correlations between operators creating a static color source in the fundamental representation of SU(3), connected via a gauge covariant parallel tranporter to a source in the $\bar{3}$ representation. The gauge connector can be formed by any sum of path-ordered products of link variables that respects the symmetry of rotations about the inter-source axis. Better ground-state operators are formed by using stout-smeared link variables in the path-ordered connec-

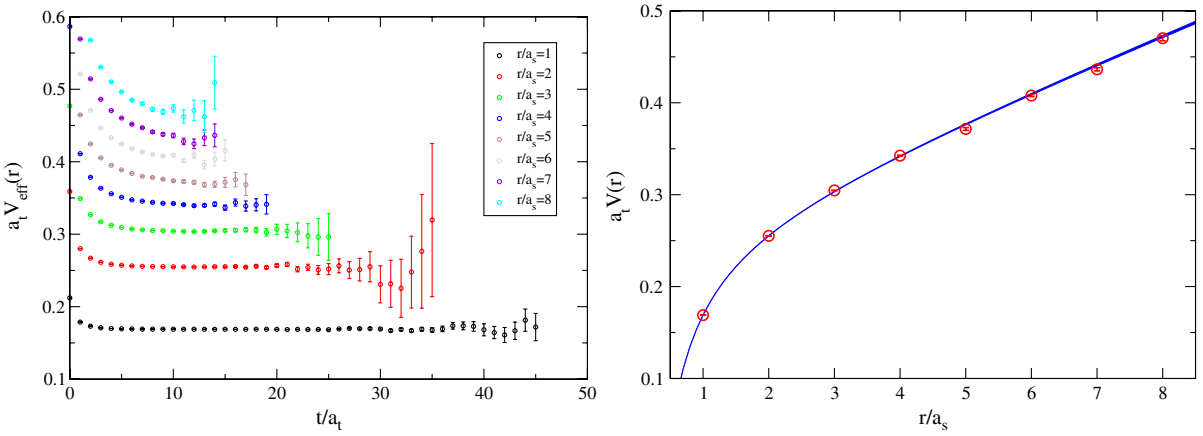

FIG. 10 (color online). Results for the static-quark potential for the $a_t m_l = -0.0808$, $a_t m_s = -0.0743$ mass set. The left panel shows the effective energies, $a_t V_{\text{eff}}(r)$ for each r. The right panel shows the resulting fit to the potential using Eq. (20).

tions and by using an operator optimized using the variational method.

A basis of five operators is constructed from the set of straight connectors and staples linking the midpoint between the two color sources. In forming the temporal correlators, straight, unsmeared temporal links are used for the propagator of the static source. A five-by-five correlation matrix $G_{ij}(r, t)$ is then computed for a range of time separations t and values of $r \in \{1, N_x/2\}$ along a lattice axis. As outlined in the previous section, this correlation matrix can be analyzed using the variational method to make a more reliable ground-state energy extraction.

Once the potential energy for a range of values of r has been determined, the data are compared with the Cornell model

$$V(r) = V_0 + \frac{\alpha}{r} + \sigma r, \tag{20}$$

and best-fit values for the parameters α, σ and V_0 are determined. See an example from one of our ensembles ($a_t m_l = -0.0808$ and $a_t m_s = -0.0743$) in Fig. 10. In all cases, a small range of r values that span r_0 are used. Once values of these parameters are computed, a value of r_0 was derived from Eq. (19). The QCD flux tube is expected to break in the presence of dynamical quarks and the ground state of the system should not be modeled by the Cornell potential at large separations. We fit the data to Eq. (19) in a sufficiently small range of r such that this issue does not arise. No good evidence of this ''string-breaking'' effect was observed in our data at larger separations. This observation fits with previous investigations [30], which established the need to include appropriate operators that construct two disconnected static-source–light-quark systems to measure the full spectrum.

IV. CHOOSING THE BARE STRANGE-QUARK MASS

The appropriate value for the strange-quark mass in the lattice action is not known *a priori*. The Wilson formulation makes the task of choosing a sensible value for this parameter more difficult, as the breaking of chiral symmetry at the action level induces an additive mass renormalization. In dynamical simulations, changes to the strange-quark mass parameter in the action cause all observables to change. We suggest that a helpful starting point for solving this issue is to determine where reference simulations lie in a parameterized two-dimensional coordinate system. Note that to leading order in chiral perturbation theory, the pseudoscalar masses are related to the quark masses via

$$m_P^2 = 2B(m_{q_1} + m_{q_2}), \tag{21}$$

where B is a low-energy constant and m_{q_i} are the quark masses that compose the meson. The light-quark dependence can be eliminated using the linear combination $(2m_K^2 - m_\pi^2)$. A useful property of a new coordinate system would be to remove all explicit dependence on the lattice cutoff. Such a dependence can be suppressed (if not completely removed) by taking ratios of hadron masses. One good candidate is the Ω baryon mass, which is stable against QCD decays and which has a simplified chiral extrapolation due to its lack of light valence quarks. An alternative is the $\Xi(1/2)$, which also decays only weakly and is statistically clean to measure. Appendix A shows a comparison between these two choices. Therefore, we suggest two dimensionless coordinates, l_Ω and s_Ω:

$$l_\Omega = \frac{9m_\pi^2}{4m_\Omega^2}, \tag{22}$$

$$s_\Omega = \frac{9(2m_K^2 - m_\pi^2)}{4m_\Omega^2}, \tag{23}$$

where the factor of $9/4$ is a convenient normalization, which makes $l_\Omega = s_\Omega = 1$ in the static-quark limit. Note that three-flavor-degenerate theories lie on the diagonal line across the unit square. Table IX summarizes all the $\{l, s\}_\Omega$ values calculated in this work. Hadron masses are taken from Tables VI and VII in Sec. V.

In Fig. 11, we locate all the simulations performed in this work using their $l_\Omega - s_\Omega$ coordinates. The dashed line

TABLE IX. Values of l_Ω and s_Ω.

N_s	N_t	$a_t m_l$	$a_t m_s$	l_Ω	s_Ω	$a_t m_\pi$	$a_t m_K$	$a_t m_\Omega$	$a_t m_\phi$
12	96	−0.0540	−0.0540	0.564(14)	0.564(14)	0.2781(9)	0.2781(9)	0.556(7)	0.334(3)
12	96	−0.0699	−0.0540	0.356(8)	0.535(10)	0.1992(17)	0.2227(15)	0.501(4)	0.3031(18)
12	96	−0.0794	−0.0540	0.214(6)	0.532(11)	0.1393(17)	0.1841(13)	0.452(5)	0.268(3)
12	96	−0.0826	−0.0540	0.148(6)	0.498(13)	0.1144(19)	0.1691(17)	0.447(5)	0.266(3)
16	96	−0.0826	−0.0540	0.161(9)	0.539(20)	0.113(3)	0.1669(15)	0.423(8)	0.258(3)
12	96	−0.0618	−0.0618	0.549(19)	0.549(19)	0.2322(15)	0.2322(15)	0.470(8)	0.286(5)
16	128	−0.0743	−0.0743	0.397(7)	0.397(7)	0.1483(2)	0.1483(2)	0.353(3)	0.2159(6)
16	128	−0.0808	−0.0743	0.231(6)	0.384(11)	0.0996(6)	0.1149(6)	0.311(6)	0.1901(18)
16	128	−0.083	−0.0743	0.154(4)	0.363(8)	0.0797(6)	0.1032(5)	0.304(3)	0.1845(11)
16	128	−0.0840	−0.0743	0.124(4)	0.367(10)	0.0691(6)	0.0970(5)	0.294(4)	0.1788(13)
24	128	−0.0840	−0.0743	0.1205(15)	0.363(4)	0.0681(4)	0.0966(3)	0.2945(16)	0.1788(6)

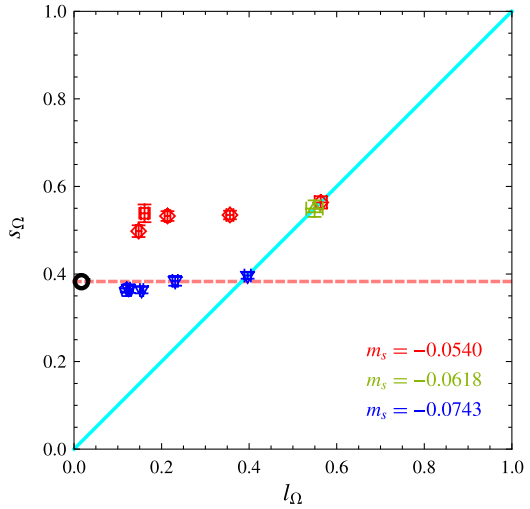

FIG. 11 (color online). The location of the dynamical ensembles used in this work in the $s_\Omega - l_\Omega$ plane. The circle (black) indicates the physical point $\{l_\Omega^{\text{phys}}, s_\Omega^{\text{phys}}\}$. The (red) diamonds and squares are generated on $12^3 \times 96$ and $16^3 \times 96$ lattices with $a_t m_s = -0.0540$; the (green) upper triangle is the ensemble on a $12^3 \times 96$ lattice with $a_t m_s = -0.0618$ and (blue) upside-down triangles and pentagons represent the ensembles on $16^3 \times 128$ and $24^3 \times 128$ lattices with $a_t m_s = -0.0743$. Detailed parameters can be found in Table IX. The horizontal dashed (pink) line indicates constant s_Ω from the physical point and the diagonal line indicates three-flavor degenerate theories.

runs horizontally from the physical point. We add two more strange-mass candidates -0.0618, -0.0743, which are the points on the diagonal line. The choice of -0.0743 seems to anchor the correct m_s value for $N_f = 3$ within one standard deviation of physical. Since we expect only a few percent deviation coming from the next-to-leading effects on s_Ω, we settle on $a_t m_s = -0.0743$ for our final choice of strange bare mass; the points to the left of the $N_f = 3$ points are $N_f = 2 + 1$ points with fixed strange input parameters. At the lightest simulation point, s_Ω only differs from $N_f = 3$ by less than 2σ. The running of the quantity s_Ω is indeed small and is thus a good means for tuning the strange-quark mass for fixed-β simulation. We note however, that the trajectory followed by simulations as bare lattice parameters are changed is dependent on the details of the lattice action and is not universal; different actions may follow different paths as their bare parameters change.

V. EXTRAPOLATION TO THE PHYSICAL QUARK MASSES

Following the discussion in Sec. IV, we adopt the coordinates l_Ω and s_Ω to perform extrapolation of the meson and baryon masses. To avoid the ambiguity in the lattice-spacing determination, we extrapolate mass ratios $\frac{a_t m_H}{a_t m_\Omega}$ using the simplest ansatz consistent with leading-order chiral effective theory,

$$\left(\frac{m_H}{m_\Omega}\right)^n = c_0 + c_l l_\Omega + c_s s_\Omega, \tag{24}$$

with $n = 2$ for pseudoscalar mesons and $n = 1$ for all other hadrons. With such a parameterization, care is needed to take account of the statistical errors of l_Ω and s_Ω in the fit.[1] Consider a general fit of the form $f = a + bx + cy$, where f, x, and y are all quantities with statistical error. We wish to find the combination of a, b, c, which minimizes

$$\sum_i \frac{(f(a, b, c; x_i, y_i) - \langle f_i \rangle)^2}{\sigma_{f_i}^2 + b^2 \sigma_{x_i}^2 + c^2 \sigma_{y_i}^2}, \tag{25}$$

where i indexes different data points $\{x, y, f\}$, $\langle \ldots \rangle$ indicates a mean over all configurations and σ is the statistical error of each quantity. The extrapolation [minimizing a quantity as in Eq. (25) with $f = \frac{m_H}{m_\Omega}$, $x = l_\Omega$ and $y = s_\Omega$] is taken to physical $\{l, s\}_\Omega$, and we then take m_Ω as experimental input to make physical predictions.

A. Hadrons

The χ^2/dof for the fits of hadronic data are all around or smaller than 1 for both meson and baryon masses. Figures 12 and 13 show the "sliced" plots of selected mass ratio with fixed l_Ω (or s_Ω). The s_Ω are almost a constant for the same sea $a_t m_s$; this is why we see almost a single extrapolated line in the left column of the figures. The hadron masses linearly increase with l_Ω and decrease with s_Ω. The ratio of m_Ξ/m_Ω is almost constant with respect to s_Ω, indicating its insensitivity to the sea strange mass. The strange-mass dependence is almost completely canceled out in such a combination. Later in Appendix A, we see the quantity $(2m_K^2 - m_\pi^2)/m_\Xi^2$ is relatively constant with respect to changes in m_π^2.

Figure 14 and the first column in Table X summarize all of our extrapolated masses along with the experimental values. The second half of the plots shows the relative discrepancy in percent between our calculation and the experimental numbers. The meson sector appears to have good agreement with experiment; overall, 0.1–4.3% discrepancy from experimental values. The biggest discrepancy comes in the η, which we estimate using a combination of light and strange pesudoscalar mesons. All the vector mesons are in good consistency with experiment; the ρ meson is only 1.2σ away. These vector mesons are below the decay threshold on our ensemble; no decays are observed. The extrapolated scalar meson a_0 is consistent with the resonance at 980 MeV. The b_1 meson is slightly higher than a_1, and both of them are 2–3σ away from experiment.

The baryon sector, on the other hand, does not work as well as the meson extrapolation. Nonstrange baryons, such

[1]Similar ratios for extrapolation were also adopted by Ref. .

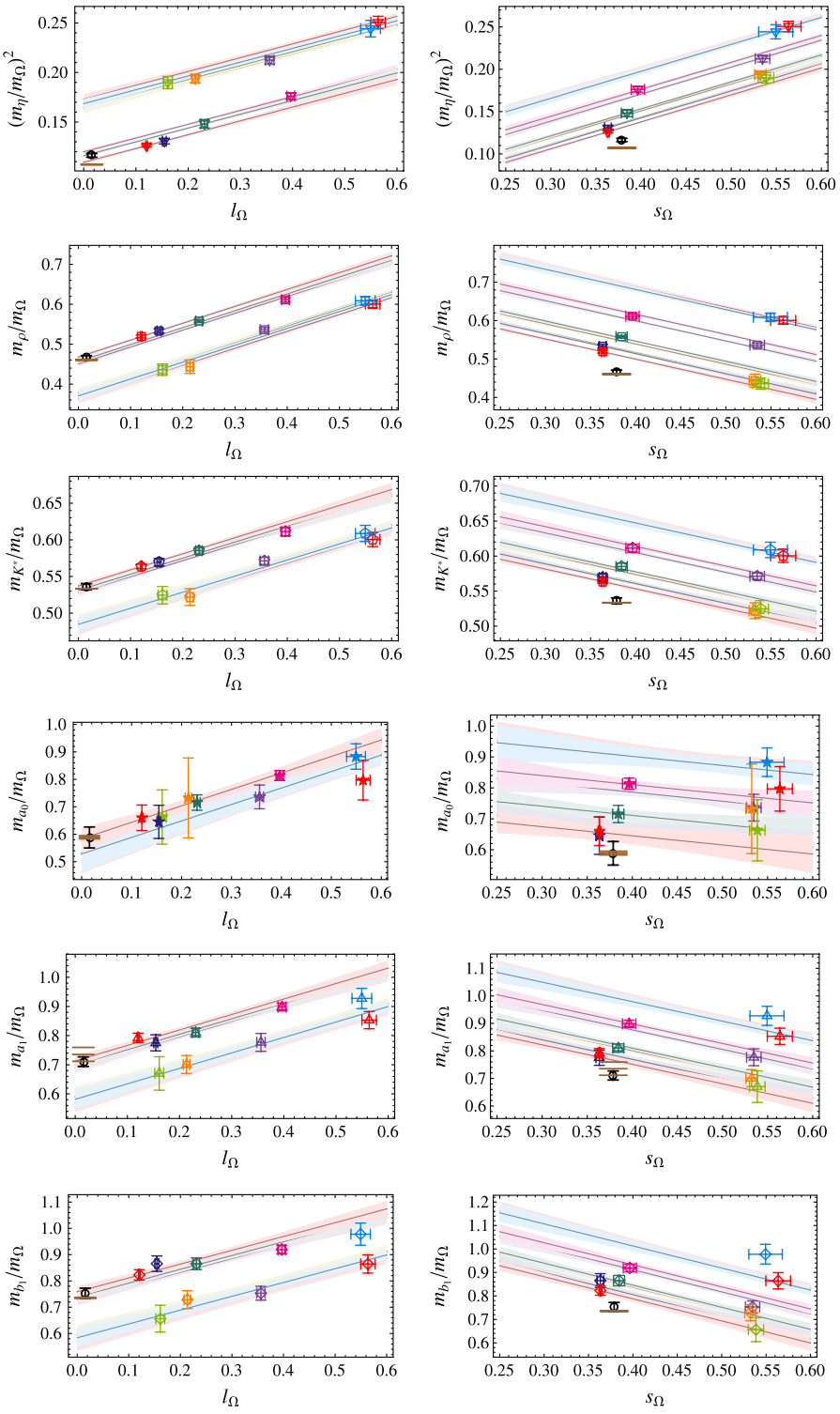

FIG. 12 (color online). Selected meson mass ratios as functions of l_Ω and s_Ω. Differently shaded (or colored) points correspond to the $a_t m_{l,s}$ combinations in Fig. 15; detailed numbers can be found in Table VI. The smaller-volume ensembles $\{a_t m_l, a_t m_s\} = \{-0.0826, -0.0540\}$ and $\{-0.0840, -0.0743\}$ are excluded from the fits. The lines indicate the "projected" leading chiral extrapolation fit in l_Ω and s_Ω, while keeping the other one fixed. The black (circular) point is the extrapolated point at physical l_Ω and s_Ω.

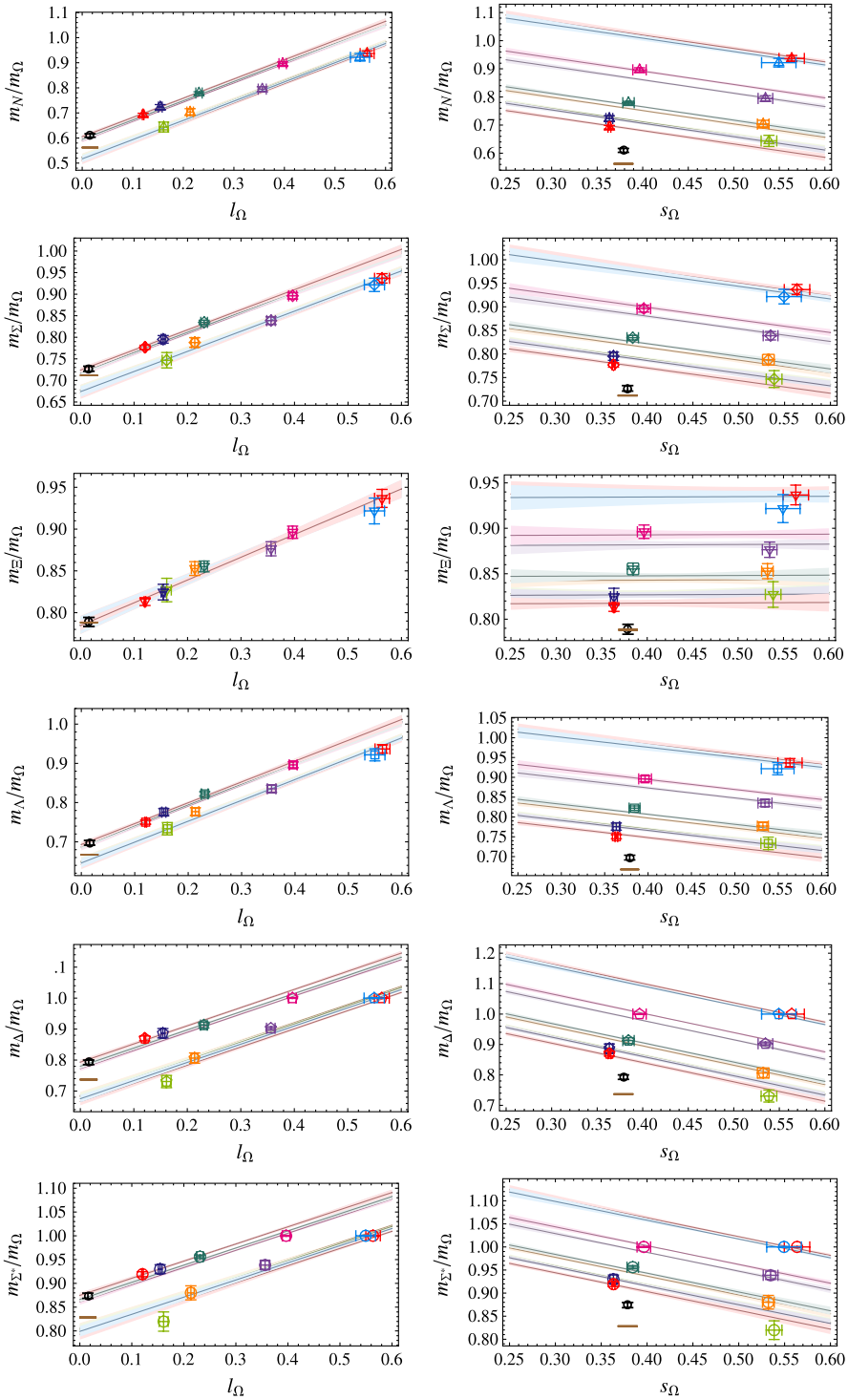

FIG. 13 (color online). Selected baryon mass ratios as functions of the l_Ω and s_Ω. Differently shaded (or colored) points correspond to the $a_t m_{l,s}$ combinations in Fig. 15; detailed numbers can be found in Table VII. The smaller-volume ensembles $\{a_t m_l, a_t m_s\} = \{-0.0826, -0.0540\}$ and $\{-0.0840, -0.0743\}$ are excluded from the fits. The lines indicate the "projected" leading chiral extrapolation fit in l_Ω and s_Ω, while keeping the other one fixed. The black (circular) point is the extrapolated point at physical l_Ω and s_Ω.

as nucleon and Delta, have the biggest discrepancy, by as much as 8.5σ. This is likely due to contributions from next-to-leading-order chiral perturbation theory (or pion-loop contributions), which are not as negligible as the meson ones. This becomes evident as we increase the number of strange quarks in the baryon: the discrepancy

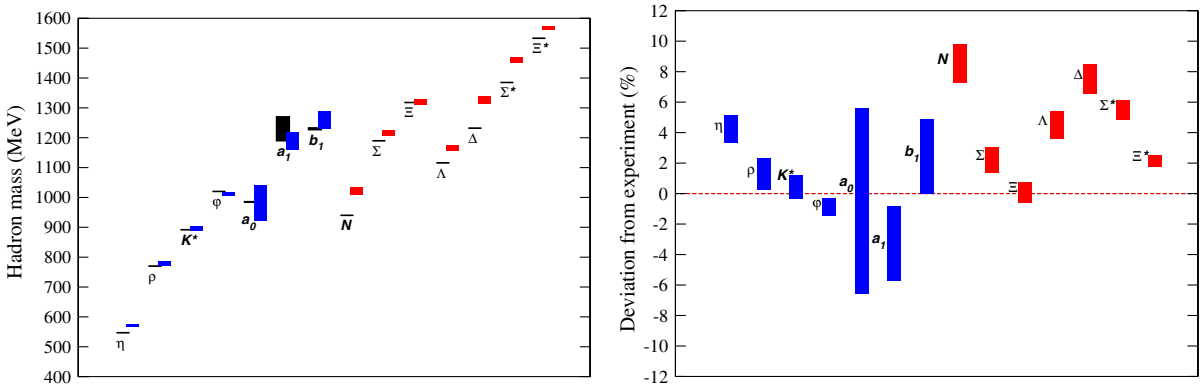

FIG. 14 (color online). Summary of the extrapolated hadron masses compared with their experimental values.

is smaller in the Sigma and cascade. To have better control of the chiral extrapolation to higher order, we must have better statistics on these measurements; this will be a task for the near future once we complete all of our gauge generation.

Finally, we compare the extrapolation results using all $a_t m_s$ ensembles and using a single ensemble of either $a_t m_s = -0.0540$ or $a_t m_s = -0.0743$ alone; results are summarized in Table X. In both cases, the ϕ measurements are in good agreement with experiment; this is expected once Ω is fixed to 1.672 GeV. However, the kaon masses from the $a_t m_s = -0.0540$ ensemble are almost 17% away from experimental ones. This is also not surprising since the $a_t m_s = -0.0540$ ensemble was selected using the J parameter strange-quark mass setting, where MILC had seen a 14–25% discrepancy in the strange-quark mass tuning. The kaon mass from the $a_t m_s = -0.0743$ ensemble, on the other hand, is only 3σ away from the physical one, which is relatively close for a tuning using degenerate light and strange masses. The extrapolations using $a_t m_s = -0.0743$ alone versus all $a_t m_s$ ensembles are in rough agreement within a few σ, indicating that $a_t m_s = -0.0743$ is a good candidate for gauge generation.

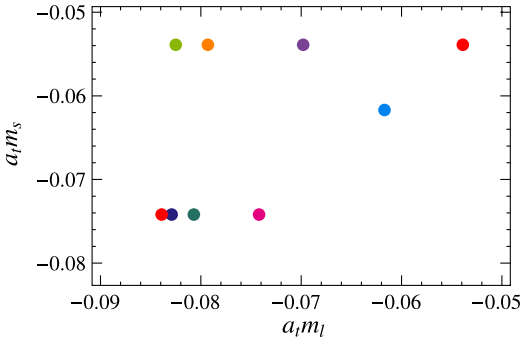

FIG. 15 (color online). The assignment of colors from different ensembles in coordinates $a_t\{m_l, m_s\}$. The convention will remain consistent when used again for later extrapolations.

TABLE X. Hadron masses (in GeV) obtained from $(m_H/m_\Omega)^n$ ($n = 2$ for pseudoscalar mesons and 1 for the other hadrons) extrapolations using different sea-strange ensembles. The square brackets indicate the χ^2/dof for each fit (with dof = 6), and the second parentheses indicate the percent deviation of the central value from experimental values.

	all	$a_t m_s = -0.0743$	$a_t m_s = -0.0540$
m_K	n/a	0.476(6)[0.14](3.74)	0.578(13)[0.17](16.7)
m_n	0.570(5)[0.04](4.29)	0.546(5)[0.25](0.2)	0.677(12)[0.62](23.79)
m_p	0.780(8)[0.72](1.27)	0.812(8)[0.12](5.4)	0.64(3)[2.96](16.52)
m_{K^*}	0.896(7)[0.49](0.5)	0.912(7)[0.1](2.27)	0.828(20)[1.7](7.19)
m_ϕ	1.011(6)[0.42](0.84)	1.012(7)[0.15](0.75)	1.007(18)[0.97](1.3)
m_{a_0}	0.98(6)[0.3](0.13)	0.98(7)[0.11](0.49)	1.06(17)[0.05](7.73)
m_{a_1}	1.19(3)[0.7](3.39)	1.23(3)[1.1](0.1)	1.03(7)[0.09](16.17)
m_{b_1}	1.26(3)[1.09](2.28)	1.33(4)[0.41](8.47)	1.03(7)[0.53](16.18)
m_p	1.020(12)[0.49](8.48)	1.033(13)[0.26](9.87)	0.93(3)[0.43](0.72)
m_Σ	1.216(10)[0.62](2.15)	1.226(11)[0.98](3.03)	1.16(2)[0.5](2.74)
m_Ξ	1.319(9)[0.8](0.08)	1.309(11)[0.63](0.69)	1.334(20)[0.62](1.22)
m_Λ	1.166(10)[1.18](4.51)	1.167(12)[1.57](4.56)	1.13(2)[0.53](1.27)
m_Δ	1.325(12)[0.97](7.57)	1.367(15)[0.36](10.93)	1.16(2)[4.81](5.78)
m_{Σ^*}	1.461(9)[1.07](5.52)	1.491(9)[0.4](7.67)	1.34(2)[2.47](3.06)
m_{Ξ^*}	1.566(6)[1.](2.17)	1.582(5)[0.84](3.16)	1.506(18)[1.81](1.79)

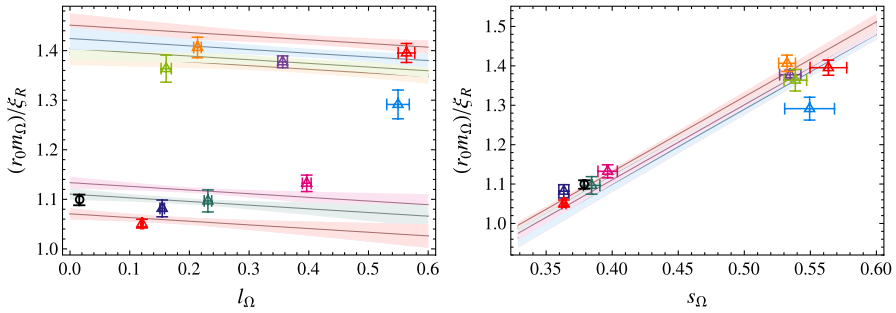

FIG. 16 (color online). "Slices" of $r_0 m_\Omega/\xi_R$ as functions of l_Ω (left) and s_Ω (middle). The straight lines are the fitted functions according to Eq. (25). The assignment of colors is shown in the Fig. 15.

B. Sommer scale at the physical quark masses

Using the static-potential data in Table VIII, we can extrapolate $r_0 m_\Omega$ to the physical limit using $\{l, s\}_\Omega$ coordinates and the simplest functional form

$$r_0 m_\Omega = f_0 + f_l l_\Omega + f_s s_\Omega. \tag{26}$$

Once this parameterization is known, m_Ω serves as experimental input and r_0 becomes a physical prediction. Using this technique, we determine the Sommer scale in the physical limit, r_0^{phys}. We compose a dimensionless ratio $\frac{r_0}{a_s}(a_t m_\Omega)$ and extrapolate using Eq. (25). After a chiral extrapolation including all three strange ensembles, we find the dimensionless ratio $r_0 m_\Omega/\xi_R = 1.100(11)$. The "sliced" fits projected on to a single parameter l_Ω (left) and s_Ω (right) at each point are shown in Fig. 16. Then we substitute in the physical Omega mass to find

$$r_0^{\text{phys}} = 0.454(5)\ \text{fm}, \tag{27}$$

with $\chi^2/\text{dof} = 1.5(0.7)$ and $\text{dof} = 6$. The biggest χ^2 contribution comes from the $a_t m_s = -0.0618$ ensemble. If we drop it, we improve χ^2/dof to 0.92(0.60) but find only a small change to $r_0^{\text{phys}} = 0.451(5)$ fm. Extrapolating using a ratio with m_ϕ rather than m_Ω gives $r_0^{\text{phys}} = 0.446(4)$ fm. These data are consistent with the MILC result in Ref. [32], which gave a continuum-extrapolated value of 0.462 (12) fm.

C. Scale setting

We determined the lattice cutoff (in physical units) at the physical point. Again, we follow the strategy of using the Omega-baryon to set the scale in physical units. A best fit of all simulation data to the model

$$a_t m_\Omega = d_0 + d_l l_\Omega + d_s s_\Omega \tag{28}$$

has $\chi^2/\text{dof} = 3.10$. Inputting the physical coordinates $\{l_\Omega, s_\Omega\} = \{0.0153, 0.379\}$ yields $a_t = 0.035\,06(23)$ fm and $a_s = 0.1227(8)$ fm.[2] The low quality of the fit provides us with further incentive to avoid expressing the lattice cutoff scale in physical units except in an extrapolation to the continuum. No continuum extrapolation is possible with our current data set, since all our ensembles have a common value of the gauge coupling β.

VI. CONCLUSION AND OUTLOOK

This paper presents our first investigation of a number of states in the light hadron spectrum of QCD with $N_f = 2 + 1$ dynamical flavors. Simulations were performed on anisotropic lattices with the ratio of spatial and temporal scales fixed nonperturbatively to $a_s/a_t = 3.5$.

The focus of this work has been to test a simple method for determining the bare strange-quark mass, to allow us to approach the physical theory. Conventionally, this has been difficult to achieve, as there is delicate coupling between lattice action parameters and the cutoff scale. We found it extremely useful to introduce a pair of coordinates, s_Ω and l_Ω to parameterize the two-dimensional space of quark mass values. The degenerate three-flavor theory corresponds to the line $l_\Omega = s_\Omega$. To leading order in the chiral effective theory, these two coordinates are proportional to the strange- and light-quark masses. These coordinates have been shown to be useful for our simulations since s_Ω shows mild dependence on changes to the lattice light-quark mass. This shows that a good approximate value of the strange quark mass can be found by following the three-flavor degenerate line to the point where s_Ω takes its physical value before changing the light-quark masses, a strategy adopted in this calculation.

With a lattice strange-quark mass close to the physical value, a number of the simplest light hadrons were investigated. The finite-volume effects for the mesons were checked on our data sets and found to be mild. Of the states we investigated, the a_0, a_1, and b_1 mesons could have decayed on our lattices. However, checking the overlap

[2]Using the values of a_t set by m_Ω at the physical point, we estimate the range of pion masses to be 0.62 to 1.52 GeV for the heaviest strange ($m_s = -0.0540$) ensembles, 1.3 GeV for the $m_s = -0.0618$ ones and 0.37 to 0.81 GeV for the $m_s = -0.0743$ ones.

factors of the interpolating operators with the ground states on different volumes suggests that the states we measured are predominantly resonances. For the octet and decuplet baryons, a similar analysis predicts that the Δ, Σ^*, and Ξ^* are stable in our study. At the heavy strange-quark masses where calculations on 12^3 lattices were performed, some finite-volume effects were seen, but they were negligible on the larger lattice volumes.

Physical predictions have been made by extrapolating simulation data as a function of these coordinates to the physical point, $\{l_\Omega, s_\Omega\} = \{0.0153, 0.379\}$. These extrapolations have been seen to be robust and have the advantage of making no reference to the lattice cutoff. This should enable reliable contact with chiral effective theories to be made. In this analysis, only the most naive extrapolations have been performed, and some discrepancy between extrapolated hadron masses and experimental data remains. It is encouraging to note that at worst, this discrepancy is less than 5% for mesons. The largest mismatch occurs in the nucleon-mass determination, which disagrees with experiment by 8%. It is very likely that the use of a naive extrapolation is responsible. No extrapolation to the continuum limit has been carried out; at present, calculations at a single value of the gauge coupling β have been performed, so no such analysis is possible.

The collaboration has begun to explore more challenging measurements on the ensembles described in this work. The anisotropic lattice should allow us to resolve heavier excited states and those states that have traditionally been statistically rather imprecise with better accuracy. These more difficult calculations include the hybrid and isoscalar mesons, including the glueballs. We are confident that a detailed picture of a broad range of light-hadron physics will emerge soon from these analyses.

ACKNOWLEDGMENTS

This work was done using the CHROMA software suite [33] on clusters at Jefferson Laboratory using time awarded under the USQCD Initiative. We thank Andreas Stathopoulos and Kostas Orginos for implementing the EigCG inverter [27] in the CHROMA library, which greatly sped up our calculations. This research used the resources of the National Center for Computational Sciences at Oak Ridge National Laboratory, which is supported by the Office of Science of the Department of Energy under Contract No. DE-AC05-00OR22725. In particular, we made use of the Jaguar Cray XT facility, using time allocated through the U.S. DOE INCITE program. This research was supported in part by the National Science Foundation under Contract Nos. NSF-PHY-0653315 and NSF-PHY-0510020 through TeraGrid resources provided by Pittsburgh Supercomputing Center (PSC), San Diego Supercomputing Center (SDSC), and the Texas Advanced Computing Center (TACC). In particular, we made use of the BigBen Cray XT3 system at PSC, the BlueGene/L system at SDSC, and the Ranger Infiniband Constellation Cluster at TACC. J. B., J. F. and C. M. were supported by Grant Nos. NSF-PHY-0653315 and NSF-PHY-0510020; E. E. and S. W. were supported by DOE Grant No. DE-FG02-93ER-40762; N. M. was supported under Grant No. DST-SR/S2/RJN-19/2007. M. P. and S. R. were supported by the Science Foundation Ireland under research Grant Nos. 04/BRG/P0275, 04/BRG/P0266, 06/RFP/PHY061, and 07/RFP/PHYF168. M. P. and S. R. are extremely grateful for the generous hospitality of the theory center at TJNAF while this research was carried out. This work was supported by DOE Contract No. DE-AC05-06OR23177, under which Jefferson Science Associates, LLC, operates Jefferson Laboratory. The U.S. Government retains a nonexclusive, paid-up, irrevocable, world-wide license to publish or reproduce this manuscript for U.S. Government purposes.

APPENDIX A: ALTERNATIVE POSSIBILITIES FOR $\{l, s\}_X$

In this work, we have been using the dimensionless parameters $\{l, s\}_\Omega$ [defined in Eq. (22)] to set the strange-quark mass and to extrapolate hadron mass ratios. In this section, we discuss alternatives to the Ω: 1). the strange vector meson ϕ, which like the Ω contains no valence up or down quarks; 2). the octet Ξ, which is statistically cleaner to measure than the decuplet Ω; 3). a linear combination of octet baryons, $2\Xi - \Sigma$, where the linear combination is selected to hopefully cancel out the leading-order up/down-quark dependence.

We first look at the s_X dependence on the sea strange mass, a similar strategy as described in Sec. IV. Figure 17 is a similar to Fig. 11, which we used to tune the sea strange quarks. The blue upside-down triangles ($V = 16^3$) and pentagon (24^3) are points from the $a_t m_s = -0.0743$ ensembles, the red diamonds ($V = 12^3$) and squares (16^3) are from $a_t m_s = -0.0540$ and the green triangles are from $a_t m_s = -0.0618$. The leftmost plot corresponds to $X = \phi$, and it shows the strong dependence of s_X on $a_t m_s$ that we are looking for to tune the strange-quark mass. The $X = \phi$ could be an alternative for setting the strange quark mass. This result also agrees with our choice of sea strange at $a_t m_s = -0.0743$. The results from s_Ξ (middle plot) show negligible sea strange dependence on $N_f = 2 + 1$; this makes it a poor index for tuning the bare strange quark, since we cannot distinguish when sea quarks are not degenerate anymore. Somehow the remaining freedom of the light quark in the Ξ baryon dominates the chiral behavior, since the $a_t m_s = -0.0743$ set is running up toward the physical line. This running is greatly improved when we consider $X = 2\Xi - \Sigma$, which lies on the physical line for all l_X. However, it is a poor candidate for tuning, since it shows little dependence on s_X.

Let us move on to how the extrapolation behavior depends on the choice of X. Table XI summarizes the results for all choices of X. The extrapolation [performed accord-

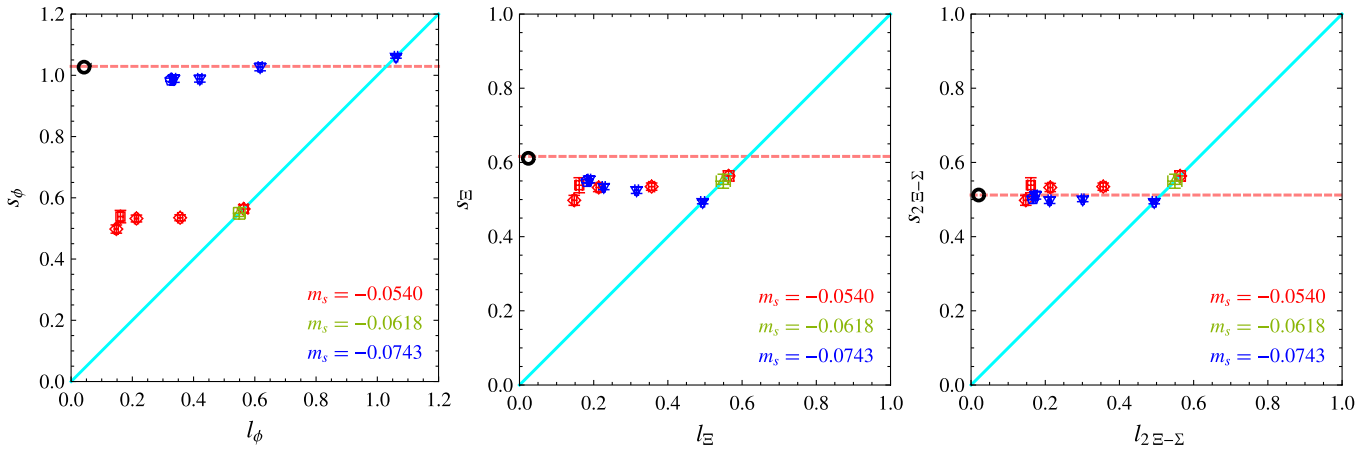

FIG. 17 (color online). The $s_X - l_X$ plot with $X = \phi$ (left) Ξ (middle) and the linear combination $2\Xi - \Sigma$ for $N_f = 3$ and $N_f = 2 + 1$ at $\beta = 1.5$. The circle (black) indicates the physical point $\{l_X^{\rm phys}, s_X^{\rm phys}\}$. The (red) diamonds and squares are $12^3 \times 96$ and $16^3 \times 96$ from $a_t m_s = -0.0540$ ensembles; (green) upper triangles are from $12^3 \times 96$ from $a_t m_s = -0.0618$ and (blue) upside-down triangles and pentagons are from $16^3 \times 128$ and $24^3 \times 128$ from $a_t m_s = -0.0743$ ensembles. Detailed parameters can be found in Table IX. The horizontal dashed (pink) line indicates physical s_X, and the straight diagonal lines indicate the SU(3) limit.

ing to the minimization process described in Eq. (25)] uses all three $a_t m_s$ ensembles without the smaller volume on the lightest ensemble of $a_t m_s = -0.0540$ and $a_t m_s = -0.0743$ sets. The $X = 2\Xi - \Sigma$ has the poorest χ^2/dof among them all; we will throw it away for reliable extrapolation comparison. The $X = \Xi$ fits have similar χ^2/dof to the ϕ but slightly worse. This is possibly due to its insensitivity to s_Ξ during the extrapolation. The $X = \phi$ should be quantitatively comparable to $X = \Omega$ coordinates. However, due to the lightness of the ϕ mass, it is not difficult to see that the next-leading-order contributions to the extrapolation form would be larger than the $X = \Omega$, causing it to be a slightly poorer fit at leading order. Even though the fit using $X = \phi$ has a smaller statistical error, we expect the systematic error to be higher than $X = \Omega$. We will leave estimation of the systematics to future precision calculations where statistical error will be more reasonable. Still, we see good consistency between $X = \phi$ and $X = \Omega$ results, which reinforces our belief in the stability of extrapolations using the dimensionless coordinates $\{l, s\}_\Omega$.

APPENDIX B: STRANGE-SETTING COMPARISONS

The J parameter [34] is one common way to set the strange-quark mass; it is defined as

$$J = \frac{dm_V}{dm_P} = \frac{m_{K^*}(m_\phi - m_\rho)}{2(m_K^2 - m_\pi^2)}. \tag{B1}$$

TABLE XI. Hadron masses (in GeV) obtained from $(m_H/m_X)^n$ ($n = 2$ for pseudoscalar mesons and 1 for the other hadrons) extrapolations in terms of $\{l, s\}_X$ with $X \in \{\Omega, \phi, \Xi, 2\Xi - \Sigma\}$ using all sea-strange ensembles. The square brackets indicate the χ^2/dof on the fit and the second parentheses denote the central value deviations from experimental values in percent.

	$X = \Omega$	$X = \phi$	$X = \Xi$	$X = 2\Xi - \Sigma$
$a_t m_\eta$	0.570(5)[0.04](4.29)	0.569(2)[0.14](4.04)	0.570(3)[0.1](4.2)	0.569(3)[0.11](4.1)
$a_t m_\rho$	0.780(8)[0.72](1.27)	0.795(5)[2.08](3.21)	0.785(7)[2.44](1.93)	0.819(7)[3.95](6.31)
$a_t m_{K^*}$	0.896(7)[0.49](0.5)	0.907(3)[1.77](1.69)	0.905(5)[2.3](1.42)	0.933(5)[3.73](4.55)
$a_t m_\phi$	1.011(6)[0.42](0.84)	n/a	1.023(5)[1.92](0.32)	1.044(5)[3.](2.32)
$a_t m_{a_0}$	0.98(6)[0.3](0.13)	0.99(6)[0.29](0.35)	0.97(7)[0.33](1.98)	1.00(7)[0.31](1.6)
$a_t m_{a_1}$	1.19(3)[0.7](3.39)	1.21(3)[0.76](2.02)	1.18(3)[1.42](3.88)	1.23(3)[1.73](0.32)
$a_t m_{b_1}$	1.26(3)[1.39](2.28)	1.28(3)[1.85](4.06)	1.27(3)[1.9](2.89)	1.32(3)[2.58](7.03)
$a_t m_p$	1.020(12)[0.49](8.48)	1.029(10)[0.89](9.45)	1.007(6)[0.06](7.09)	1.048(9)[0.63](11.5)
$a_t m_\Sigma$	1.216(10)[0.62](2.15)	1.226(8)[1.21](3.06)	1.211(4)[2.7](1.75)	1.243(7)[3.81](4.43)
$a_t m_\Xi$	1.319(9)[0.8](0.08)	1.323(7)[1.42](0.39)	n/a	1.345(4)[3.47](2.02)
$a_t m_\Lambda$	1.166(10)[1.18](4.51)	1.176(8)[1.86](5.38)	1.161(3)[0.54](4.06)	1.194(6)[1.6](6.97)
$a_t m_\Delta$	1.325(12)[0.97](7.57)	1.335(17)[1.38](8.36)	1.312(18)[1.68](6.51)	1.356(19)[2.66](10.07)
$a_t m_{\Sigma^*}$	1.461(9)[1.07](5.52)	1.464(15)[1.41](5.72)	1.450(15)[1.41](4.66)	1.490(17)[2.49](7.58)
$a_t m_{\Xi^*}$	1.566(6)[1.](2.17)	1.568(12)[1.03](2.3)	1.561(13)[1.15](1.8)	1.593(15)[2.22](3.94)
$a_t m_\Omega$	n/a	1.685(10)[0.37](0.8)	1.683(12)[0.89](0.64)	1.708(12)[1.82](2.17)

Here, we examine how the parameter works for setting the strange-quark mass in our calculation. The upper four points in Fig. 18 are from $N_f = 2 + 1$ at fixed $m_s = -0.0540$ and $m_l \in \{-0.0699, -0.0794, -0.0826\}$ from right to left with two volumes on -0.0826 (12^3 and 16^3). We hit the experimental value J^{exp} with the first $m_l = -0.0699$, and the remaining points are within 1σ of J^{exp}. However, when we tried to extrapolate the kaon mass (see Sec. V), we found that it missed the experimental value by about 17%. Such a mismatch resulting from tuning the strange mass using the J parameter has previously been reported in the literature. For example, MILC also found their lattice J parameter on their coarse and fine lattices agreed with J^{exp}, but after extrapolation they found the sea strange-quark mass to be off by 25% and 14% on the coarse and fine lattices, respectively [32]. Although the discrepancy seems to become smaller for finer lattices, the J parameter does not seem to be an ideal quantity for strange-quark tuning. Similar conclusions can also be reached by observing the four lower points in Fig. 18, which correspond to a $m_s = -0.0743$, $N_f = 2 + 1$ simulation; these are only two σ away from the points for $m_s = -0.0540$. The J parameter is not sensitive enough to changes in the strange sea-quark mass.

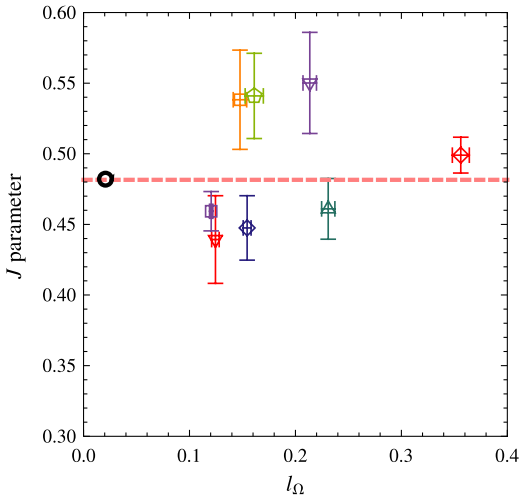

FIG. 18 (color online). J-parameter plot for $N_f = 2 + 1$ at $\beta = 1.5$. The upper diamond, upside-down triangle, pentagon ($V = 12^3 \times 96$) and square ($V = 16^3 \times 96$) points are from $m_s = -0.0540$ ensembles and the triangle, lower diamond, upside-down triangle ($V = 16^3 \times 128$) and square ($V = 24^3 \times 128$) points are from $m_s = -0.0743$; the circle (black) indicates the physical point $\{l_\Omega^{\text{phys}}, J^{\text{phys}}\}$; the dashed line indicates the physical J value.

[1] T. S. H. Lee and L. C. Smith, J. Phys. G **34**, S83 (2007).
[2] A. Matsuyama, T. Sato, and T. S. H. Lee, Phys. Rep. **439**, 193 (2007).
[3] S. Basak *et al.*, Phys. Rev. D **72**, 094506 (2005).
[4] S. Basak *et al.* (Lattice Hadron Physics Collaboration (LHPC)), Phys. Rev. D **72**, 074501 (2005).
[5] S. Basak *et al.*, arXiv:hep-lat/0609052.
[6] S. Basak *et al.*, Phys. Rev. D **76**, 074504 (2007).
[7] J. J. Dudek, R. G. Edwards, N. Mathur, and D. G. Richards, Phys. Rev. D **77**, 034501 (2008).
[8] J. J. Dudek, R. G. Edwards, and D. G. Richards, Phys. Rev. D **73**, 074507 (2006).
[9] H.-W. Lin, S. D. Cohen, R. G. Edwards, and D. G. Richards, Phys. Rev. D **78**, 114508 (2008).
[10] R. G. Edwards, B. Joo, and H.-W. Lin, Phys. Rev. D **78**, 054501 (2008).
[11] J. Foley (private communication).
[12] P. Chen, Phys. Rev. D **64**, 034509 (2001).
[13] C. Morningstar and M. J. Peardon, Phys. Rev. D **69**, 054501 (2004).
[14] R. Sommer, Nucl. Phys. **B411**, 839 (1994).
[15] M. A. Clark, Proc. Sci. LAT2006 (2006) 004.
[16] E. Remez, C.R. Hebd. Seances Acad. Sci. **199**, 337 (1934).
[17] E. Remez, *General Computational Methods of Chebyshev Approximation* (U.S. Atomic Energy Commission, Division of Technical Information, Washington, DC, 1962).
[18] B. Jegerlehner, arXiv:hep-lat/9612014.
[19] J. C. Sexton and D. H. Weingarten, Nucl. Phys. **B380**, 665 (1992).
[20] I. M. Omelyan, I. P. Mryglod, and R. Folk, Comput. Phys. Commun. **151**, 272 (2003).
[21] T. Takaishi and P. de Forcrand, Phys. Rev. E **73**, 036706 (2006).
[22] R. Morrin, A. O. Cais, M. Peardon, S. M. Ryan, and J.-I. Skullerud, Phys. Rev. D **74**, 014505 (2006).
[23] M. A. Clark and A. D. Kennedy, Nucl. Phys. B, Proc. Suppl. **140**, 838 (2005).
[24] M. A. Clark and A. D. Kennedy, Phys. Rev. Lett. **98**, 051601 (2007).
[25] C. Michael, Nucl. Phys. **B259**, 58 (1985).
[26] M. Luscher and U. Wolff, Nucl. Phys. **B339**, 222 (1990).
[27] A. Stathopoulos and K. Orginos, arXiv:0707.0131.
[28] N. Mathur *et al.*, Phys. Rev. D **70**, 074508 (2004).
[29] C. W. Bernard *et al.*, Phys. Rev. D **64**, 054506 (2001).
[30] G. S. Bali, H. Neff, T. Dussel, T. Lippert, and K. Schilling, Phys. Rev. D **71**, 114513 (2005).
[31] S. Durr *et al.*, Science **322**, 1224 (2008).
[32] C. Aubin *et al.*, Phys. Rev. D **70**, 094505 (2004).
[33] R. G. Edwards and B. Joo (SciDAC Collaboration), Nucl. Phys. B, Proc. Suppl. **140**, 832 (2005).
[34] P. Lacock and C. Michael, Phys. Rev. D **52**, 5213 (1995).